
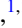




First-principles investigation of near-field energy transfer between localized quantum emitters in solids

Swarnabha Chattaraj ^{1,*} Supratik Guha ^{1,2} and Giulia Galli ^{1,2,†}

¹Materials Science Division, Argonne National Laboratory, Lemont, Illinois 60439, USA

²Pritzker School of Molecular Engineering, University of Chicago, Chicago, Illinois 60637, USA

 (Received 24 October 2023; revised 23 May 2024; accepted 18 July 2024; published 14 August 2024)

We present a predictive and general approach to investigate near-field energy transfer processes between localized defects in semiconductors, which couples first-principles electronic structure calculations and a nonrelativistic quantum electrodynamics description of photons in the weak-coupling regime. The approach is general and can be readily applied to investigate broad classes of defects in solids. We apply our approach to investigate an exemplar point defect in an oxide, the F center in MgO, and we show that the energy transfer from a magnetic source, e.g., a rare-earth impurity, to the vacancy can lead to spin nonconserving long-lived excitations that are dominant processes in the near field, at distances relevant to the design of photonic devices and ultrahigh dense memories. We also define a descriptor for coherent energy transfer to predict geometrical configurations of emitters to enable long-lived excitations, that are useful to design optical memories in semiconductor and insulators.

DOI: [10.1103/PhysRevResearch.6.033170](https://doi.org/10.1103/PhysRevResearch.6.033170)

I. INTRODUCTION

Energy transfer between localized emitters embedded in a solid host material, for example point defects, is a ubiquitous phenomenon of interest to several fields, including photonics, microelectronics, and quantum networks. Energy transfer may be mediated by several complex mechanisms, including direct tunneling, photons, and phonons. Here we focus on photon mediated transfer from source to absorber, i.e., fluorescent resonance energy transfer (FRET) or nonradiative resonance energy transfer (NRET) [1–5], and we consider the near-field regime where the source-absorber distance is smaller than the wavelength of the photons being transferred.

This regime is of interest, for example, to study quantum emitters in close proximity of each other in semiconductors and insulators [6], and/or emitters close to other impurities such as oxygen vacancies in oxide hosts. Understanding NRET phenomena is critical to gain insight into the design of solid-state rare-earth-doped quantum memories and repeaters [7], as well as, potentially, ultrahigh density classical optical memories. In particular, we envision to individually address, by optical means, narrow band rare-earth (RE) emitters [8] out of an ensemble dispersed in a solid-state host, for example an oxide, and to transfer narrow-band excitations to a proximal defect (see Fig. 1 and Appendix A). In such platforms, with a realistic few ppm doping, the average separation between REs and defects can be of the order of ~ 5 to ~ 10 nm—a distance

much smaller than the wavelength of the optical/near infrared (NIR) photons (~ 500 nm to ~ 1 μ m). Thus, NRET processes at the near-field regime play a critical role. We also envision enhancing the lifetime of the excitation transferred between the RE and a nearby defect through spin nonconserving transitions.

In the near field [1–5,9], transitions corresponding to optical absorption and emission processes have characteristics markedly different from those of electronic transitions occurring in the far-field regime and may result in violation of spin and orbital selection rules [9–12] that are valid in the far field. The ability to engineer spin- or orbital-forbidden optical absorption excitations in emitters at near field provides a pathway to significantly increase the lifetime of optical memories (Appendix A). The material systems relevant to such technologies span, in principle, a wide range including native defects [13,14] (F centers, Frenkel defects), implanted defects, and deposited dopants (rare-earth in oxides [6,7,8,15–20], NV and SiV in diamond [21–24], donor or acceptors in semiconductors), and quantum dots [25–27].

Investigating such a vast range of material systems demands a theoretical approach that allows for an efficient way to account for the symmetry, spread, and many-body nature of the wave functions of the localized emitters and hence it requires the use of first-principles electronic structure theories such as density-functional theory (DFT) [28–30], many body perturbation theories [31–33] or, if multireference states are present, more sophisticated approaches such as quantum embedding [34–37] theories and time-dependent DFT [38].

Historically the study of resonant energy transfer has developed in the field of molecular quantum electrodynamics (QED) to address energy transfer between molecules and molecular complexes [39–45]. In the solid state, NRET processes have also been explored to understand exciton diffusion, transfer, and light trapping mechanisms [3,46]. In either case, dipole-dipole approximations were often adopted, and

*Contact author: schattaraj@anl.gov

†Contact author: gagalli@uchicago.edu

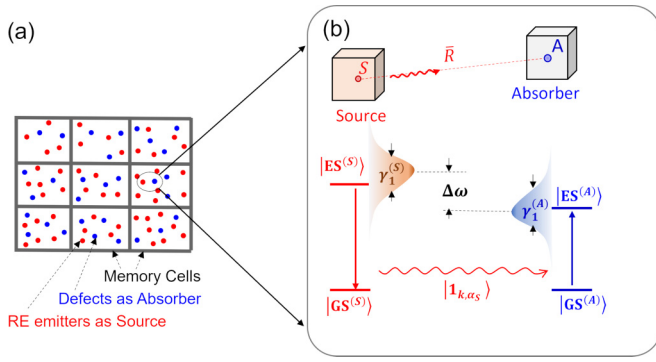


FIG. 1. (a) A schematic representation of ultrahigh density optical memories proposed here (Appendix A) where each memory-cell in a solid host contains an ensemble of rare-earth (RE) emitters (source, red) and point-defects (absorber, blue). (b) A RE emitter-defect complex representing the working “unit” of the memory. Optical excitations of RE emitters that are spectrally separated can be transferred to a suitable defect in the proximity of the emitter to trap the excitation and increase its lifetime. The source (S) and the absorber (A) are separated by distance \vec{R} . The photon propagation (curly arrow) is treated within quantum electrodynamics. The ground and excited states of S and A are labeled with GS and ES, respectively and the photon by $|1_{k,\alpha_S}\rangle$, where k indicates the photon momentum and α_S represents the set $\{L = \text{orbital angular momentum}, J_z = \text{total angular momentum projected to a chosen direction } z, P = \text{parity}\}$ specifying the multipole mode of the photon. The linewidth of the transition at finite timescale is $\gamma_1^{(S/A)} = 1/T_1^{(S/A)}$ (T_1 is the decay lifetime); due to the finite linewidth, energy transfer may occur even if energy levels are mismatched by a frequency difference $\Delta\omega$.

the matrix elements for photon absorption and emission defined phenomenologically.

On the other hand, the approach of quantum electrodynamical density-functional theory (QEDFT) [47–50] treats the light matter coupling entirely from first-principles with a full diagonalization of the electron-photon coupled system (polaritons and exciton-polaritons). Such an approach is best suited to describe a strong-coupling regime where the light-matter coupling can be comparable to the energy of the photon itself. While QEDFT enabled unique applications in polaritonic chemistry, for example polaritonic catalysis [49–50], the approach is computationally rather demanding, and it typically considers a single cavity mode coupled with localized electronic systems such as isolated molecules.

However, there are several instances of weak coupling between light and matter, in particular quantum emitters in solids, where a full polariton treatment is neither necessary nor feasible, and a perturbative approach is warranted. Here we model the light matter coupling at localized emitters in the solid state from first-principles, where the complexity of the solid host material and its interaction with the defect are taken into account. We use the Pauli Hamiltonian [51–54] to describe the light-matter coupling with the photon field operators expressed in a multipole basis [55–57]. The properties of the multipole basis are exploited to increase the efficiency of our calculations, paving the way to tackle large ensembles of defects in a condensed matter environment, which would be difficult to treat in a plane wave basis. We thus report a

general framework for the calculation of the energy transfer between localized emitters in solids, at arbitrary separation (near/ far field) where the electronic structure and light matter interaction are treated with a rigorous first-principles theory, and the propagation of the photon is treated within a quantum electrodynamical picture valid at any arbitrary distance. The approach is readily applicable to broader classes of localized emitters in any semiconducting/insulator host material. As an example, we use our approach to investigate energy transfer in a realistic system of localized defects in a typical insulating host, MgO with F centers, which are commonly found in real substrates. We consider a magnetic and an electric dipolar source emitting at near field (mimicking a rare-earth substitutional site in the host), and we investigate NRET processes as a function of the source-to-absorber distance and orientation. We also discuss configurations and criteria to obtain dominant spin-flip transitions in the near field, which are relevant for the design of classical optical memories and of quantum networks.

In the rest of the paper, we lay out the theoretical approach that integrates first-principles electronic structures, and non-relativistic QED to study NRET between arbitrary localized emitters in solids from nanometer to macroscopic separations. We then apply our approach to the F center in MgO and highlight the key differences between near-field and far-field absorption processes, and we define an effective radius for coherent transport rates and discuss its implication to device design.

II. THEORETICAL APPROACH

We start by presenting our theoretical approach to calculate the time dependent probability amplitude for the NRET between two emitters at an arbitrary separation and orientation in a solid host. We assume that the main transitions of interest to NRET between quantum emitters are those between the localized bound states of electrons within the source and the absorber [Fig. 1(b)], and do not consider any transitions between the bulk extended states [58]. We further assume that the emitters are sufficiently distant from each other so that there is no overlap between their respective electronic wave functions, and direct Coulomb interaction can be neglected. We write the Hamiltonian of the coupled emitter-photon system as

$$H = H_S + H_A + H_{\text{Field}} + H_{\text{int}}. \quad (1)$$

Here H_S and H_A are the Hamiltonians of the source S (for example a rare-earth impurity in an oxide) and absorber A (for example an oxygen vacancy in an oxide) respectively, and H_{Field} is the Hamiltonian of the photon. We define $H_0 = H_S + H_A + H_{\text{Field}}$ as the unperturbed Hamiltonian and H_{int} as the light-matter interaction perturbation on H_0 .

In general, $H_{S/A}$ are many body Hamiltonians expressed as $H_{S/A} = \sum_n \epsilon_n^{S/A} |\Phi_n^{(S/A)}\rangle \langle \Phi_n^{(S/A)}|$, where the many electron eigenstates, $|\Phi_n^{(S/A)}\rangle$ can be written as a sum of Slater determinants constructed from single electronic states $\{|\phi_i^{(S/A)}\rangle, i = 1 : N_{S/A}\}$, $N_{S/A}$ being the number of the single particle electronic states in the source S or the absorber A . These Hamiltonians include the interaction between the source and emitter and the host matrix from first prin-

ciples. The field Hamiltonian is expressed as $H_{\text{Field}} = \sum_{k, \alpha} \hbar \omega_k (a_{k, \alpha}^\dagger a_{k, \alpha} + \frac{1}{2})$, where $a_{k, \alpha}^\dagger$ is the creation operator of a photon in the mode $\{k, \alpha\}$; k is the radial wave number and α represents the set $\{L, J_z, P\}$ specifying the symmetry and polarization— L being the photon's orbital angular momentum, J_z the photon's total angular momentum (orbital and spin) projected along a chosen direction z , and P the parity. The state of the photon, emitted from the source S , is represented as a linear combination of radiating multipole modes [55–57, Appendix B] denoted by $|1_{k, \alpha_S}\rangle$. The subscript S of α indicates that the multipolar mode is defined centered around S . These modes, obtained by solving the Maxwell equations, are standing waves, with a Bessel j function as radial part, for a perfectly bound spherical cavity. For an open cavity the radial functions are instead type 1 Hankel functions [Appendix B].

We write H_{int} as

$$H_{\text{int}} = \sum_{E=S,A} \sum_{i=1}^{N_E} \left[-\frac{e \vec{p}_i \cdot \vec{A}}{2m_0} - \frac{e \vec{A} \cdot \vec{p}_i}{2m_0} + \frac{e^2 \vec{A} \cdot \vec{A}}{2m_0} + eA_0 + g \frac{e\hbar}{2m_0} \vec{\sigma}_i \cdot \vec{\nabla} \times \vec{A} \right]. \quad (2)$$

$$\begin{aligned} \vec{A}_{k, \alpha_S}(\vec{r}, t) = & \frac{1}{4\pi} \sqrt{\frac{k}{R_{\text{norm}}}} \left[\left(\sqrt{\frac{L}{2L+1}} g_{L+1}(kr) \vec{Y}_{L, L+1, J_z}(\hat{r}) + \sqrt{\frac{L+1}{2L+1}} g_{L-1}(kr) \vec{Y}_{L, L-1, J_z}(\hat{r}) \right) \right. \\ & \left. + C \left(-\sqrt{\frac{L+1}{2L+1}} g_{L+1}(kr) \vec{Y}_{L, L+1, J_z}(\hat{r}) + \sqrt{\frac{L}{2L+1}} g_{L-1}(kr) \vec{Y}_{L, L-1, J_z}(\hat{r}) \right) \right] e^{-i\omega_k t} \end{aligned} \quad (3)$$

and

$$A_{0; k, \alpha_S}(\vec{r}, t) = \frac{C}{4\pi} \sqrt{\frac{k}{R_{\text{norm}}}} g_L(kr) Y_{L, J_z}(\hat{r}) e^{-i\omega_k t}. \quad (4)$$

Here $g_L(kr) = 4\pi i^L z_L(kr)$, $z_L(kr)$ are spherical Bessel functions, $Y_{L, M}$ and $\vec{Y}_{L, L, M}$ are spherical scalar and vector harmonics respectively, and R_{norm} denotes the radius of the normalizing sphere for the multipole mode (see Appendix B for details). For a magnetic type of mode ($(-1)^L = -P$), the vector and scalar potential fields are

$$\vec{A}_{k, \alpha_S}(\vec{r}, t) = \frac{1}{4\pi} \sqrt{\frac{k}{R_{\text{norm}}}} g_L(kr) \vec{Y}_{L, L, J_z}(\hat{r}) e^{-i\omega_k t} \quad (5)$$

and

$$A_{0; k, \alpha_S}(\vec{r}, t) = 0. \quad (6)$$

The constant C is an arbitrary parameter representing gauge freedom. The choice of C does not affect the value of the matrix elements discussed below, but the computation can be simplified by choosing $C = 0$ (radiation gauge of Coulomb gauge) for which the scalar potential vanishes [Eq. (4)]. This results in a Coulomb gauge formalism in the minimal coupling form [60] in the multipolar basis. We also neglect here elastic scattering of photons represented by the $\frac{e^2 \vec{A} \cdot \vec{A}}{2m_0}$ term [54] since it does not play a role in energy transfer process. Eq. (2), derived from the generalized Kramers-Heisenberg or Pauli

Hamiltonian [51] reduces to $e\vec{E} \cdot \vec{r}$ only under specific conditions [54]: (1) resonant conditions, i.e., when the frequency of the photon matches the energy gap of the electronic states and when (2) the electronic states are eigenfunctions of a local Hamiltonian. The first criterion does not apply for NRET where significant energy transfer may occur under nonresonant conditions. In addition, in DFT calculations with hybrid functionals, nonlocal terms are introduced in the Hamiltonian, in addition to nonlocal terms present in the pseudopotentials, such as the Kleinman-Bylander projectors and the optimized Vanderbilt projectors [61]. Thus, the fully general $\vec{A} \cdot \vec{p}$ form [Eq. (2)] should be used when first-principles hybrid DFT calculations are carried out. As mentioned in the introduction, in nonrelativistic QEDFT [47–49] the Hamiltonian [Eq. (1)] is diagonalized for arbitrary light matter coupling strengths and coupled electrons and photons (polaritons and exciton-polaritons) wave functions are computed. Such an approach allows for the exploration of strong coupling regimes useful to investigating phenomena such as polaritonic catalysis [50]. However, in the case of NRET between localized defects in a bulk solid, the photon modes leak into the continuum within \sim femtosecond time scale, while light matter coupling (as measured by radiative decays) usually occurs within \sim nanosecond or longer time scales for typical emitters, including deep-levels and rare earths in semiconductors and insulators, and quantum dots. These conditions define the so-called weak coupling regime, whose description may be obtained using a perturba-

tive approach, where the unperturbed states of electrons and photons are used as basis sets for the interacting Hamiltonian of Eq. (1).

We consider an initial state where only the source S is in an excited state (ES), no photon is present in the system and the absorber is in the ground state (GS): $\Psi_i = \Psi(t=0) = |\text{ES}^{(S)}\rangle|\text{GS}^{(A)}\rangle$; after the energy is transferred from S to the absorber A, the system is in the final state $\Psi_f = |\text{GS}^{(S)}\rangle|\text{ES}^{(A)}\rangle$. The energy transfer between S and A can occur through all possible intermediate states $|I\rangle = |\text{GS}^{(S)}\rangle|\text{GS}^{(A)}\rangle|1_{k,\alpha_S}\rangle$ or $|\text{ES}^{(S)}\rangle|\text{ES}^{(A)}\rangle|1_{k,\alpha_S}\rangle$ [See Appendix G]. In these two intermediate states, the photon mode $|1_{k,\alpha_S}\rangle$ constitutes the spherical Hankel function of type (1) or type (2), respectively, to represent outward propagating and inward propagating spherical waves centered at S. Thus, the effect of retarded and advanced photon green function can be separated from the beginning by choosing the type of the Hankel function. We here take the intermediate states represented by the type 1 Hankel function to understand the energy propagation from S to A. This is different from plane wave formulation where sum of all plane wave modes automatically includes both retarded and advanced parts and a Fourier transform is needed to separate the two [4,5].

The NRET amplitude $c(t) = \langle\Psi_f|\Psi(t)\rangle$ is [4,5]

$$c(t) = \frac{2M}{\hbar} \frac{\sin\left(\frac{\Delta\omega t}{2}\right)}{\Delta\omega} e^{-\frac{t}{T_{1S}}}. \quad (7)$$

Here $\omega^{(S/A)} = \langle\text{ES}^{(S/A)}|\mathcal{H}_{(S/A)}|\text{ES}^{(S/A)}\rangle - \langle\text{GS}^{(S/A)}|\mathcal{H}_{(S/A)}|\text{GS}^{(S/A)}\rangle$ are the electron state transition energies for the source and the absorber in the solid state environment, and $\Delta\omega = \omega^{(A)} - \omega^{(S)}$ is the energy mismatch between the source and the absorber transitions as indicated in Fig. 1(b), T_{1S} is the decay rate of the isolated source, and within second-order perturbation theory, the matrix element M is expressed as a sum over all possible intermediate states:

$$M = \sum_I \frac{\langle\Psi_f|\tilde{\mathcal{H}}_{\text{int}}|I\rangle\langle I|\tilde{\mathcal{H}}_{\text{int}}|\Psi_i\rangle}{\hbar(\omega_i - \omega_I)}, \quad (8)$$

where $\tilde{\mathcal{H}}_{\text{int}}(t) = e^{\frac{i\hbar\omega_i t}{\hbar}} \mathcal{H}_{\text{int}}(t) e^{-\frac{i\hbar\omega_i t}{\hbar}}$. Here ω_I and ω_i represent the energy of the intermediate state and the energy of the initial state, respectively. For the absorption of a photon in the state $|1_{k,\alpha_S}\rangle$ resulting in an electronic transition from $|\text{GS}^{(A)}\rangle$ to $|\text{ES}^{(A)}\rangle$ at the absorber site, we define the photon absorption matrix element:

$$V_{k,\alpha_S}^{(A)} = \langle\Psi_f|\tilde{\mathcal{H}}_{\text{int}}|I\rangle = \langle\text{ES}^{(A)}|\tilde{\mathcal{H}}_{\text{int}}|\text{GS}^{(A)}, 1_{k,\alpha_S}\rangle. \quad (9)$$

Equation (9) can be simplified to an expression containing only integrals of single electron orbitals $\phi_{i/j}^{(A)}$ using the Slater-Condon rule [62, 63, Appendix C and D]:

$$V_{k,\alpha_S}^{(A)} = \langle\phi_i^{(A)}|\tilde{\mathcal{H}}_{\text{int}}|\phi_j^{(A)}, 1_{k,\alpha_S}\rangle. \quad (10)$$

Similarly, for the emission of a photon $|1_{k,\alpha_S}\rangle$ resulting from an electronic transition from the excited state $|\text{ES}^{(S)}\rangle$ to the ground state $|\text{GS}^{(S)}\rangle$, we define the matrix element:

$$V_{k,\alpha_S}^{(S)} = \langle I|\tilde{\mathcal{H}}_{\text{int}}|\Psi_i\rangle = \langle\phi_i^{(S)}, 1_{k,\alpha_S}|\tilde{\mathcal{H}}_{\text{int}}|\phi_j^{(S)}\rangle. \quad (11)$$

As shown in Appendix G, it is convenient to use the following expressions for the matrix elements $V_{k,\alpha_S}^{(S)} = v_{k,\alpha_S}^{(S)}\sqrt{\Delta k}$,

and $V_{k,\alpha_S}^{(A)} = v_{k,\alpha_S}^{(A)}\sqrt{\Delta k}$. Here Δk is the width of the mode $|1_{k,\alpha_S}\rangle$ in k space and is related to the radius of the normalizing sphere R_{norm} : $\Delta k = \pi/R_{\text{norm}}$. From Eq. (8) we have

$$M = \frac{i\pi n_i}{\hbar c} \sum_{\alpha} v_{k_S,\alpha_S}^{(S)} v_{k_S,\alpha_S}^{(A)}, \quad (12)$$

where the expression of M is general and contains all the multipolar contributions along with the absorption and emission matrix elements defined from first principles. Here n_i represents the refractive index of the host material and c the vacuum speed of light. We emphasize that Eq. (12) not only goes beyond the dipolar approximation, but also contains the interactions between the source and absorber and the solid matrix, through the calculation of the matrix elements Eqs. (10) and (11). Under the dipole approximation in the long wavelength limit the expression in Eq. (12) is consistent with $M(\bar{R}) = \bar{p}_S \cdot \bar{G}(\bar{R}) \cdot \bar{p}_A$, where \bar{G} is the electromagnetic Green function, and \bar{p}_S and \bar{p}_A are the transition dipoles at the source and the absorber. For convenience we can express the transfer amplitude $c(t)$ as a function of the mediating photon amplitude $c_k(t)$, with $c(t) = \int dk c_k(t)$, where (Appendix G)

$$c_k(t) = \frac{1}{\hbar^2} \sum_{\alpha_S} \frac{v_{k_S,\alpha_S}^{(S)} v_{k_S,\alpha_S}^{(A)}}{\omega_k - \omega_S} \times \left(\frac{e^{-i\omega_S t} - e^{-i\omega_A t}}{\omega_A - \omega_S} - \frac{e^{-i\omega_k t} - e^{-i\omega_A t}}{\omega_A - \omega_k} \right). \quad (13)$$

Equation (13) is analogous to similar expressions using a plane wave basis (for example Eq. (1) of Ref. [4]). However, here the momenta of the multipole modes are expressed by a number (k = radial momentum) and not a vector (as in plane wave basis), thus simplifying the expressions particularly for the higher order multipoles [11,12] of interest to the discussion of our results.

We note that expressing $v_{k_S,\alpha_S}^{(A)}$ and $v_{k_S,\alpha_S}^{(S)}$ from first principle allows for the study of different, interesting cases of emitters in solids: (i) emitters with electronic states localized in $< \text{nm}$ scale, which can be described using DFT [28–30], many body perturbation theories [31–35], or embedding theories [36–38]; (ii) emitters such as rare-earth substitutional sites where one can derive the associated multipoles of the transitions either from theory, including crystal field theory [64–66], or from experiments [7,8]; and (iii) emitters such as quantum dots for which the wave functions of the bound electron and hole may extend over ~ 20 nm and may be described using a single particle picture, together with our perturbative approach with higher order multipoles [67]. In addition, first-principles calculations of the matrix elements pave the way to predictive discoveries of viable defects and host platforms for optical memories and quantum networks, since we do not assume any *ad hoc* model for the source and emitters, and we consider their electronic structure within the solid.

As an example, we now turn to describe energy transfer in a well-known defect in MgO, the F center, where we assume photon sources are provided by rare-earth defects implanted in the material and pinpoint the uniqueness and the relevance of the near-field effects.

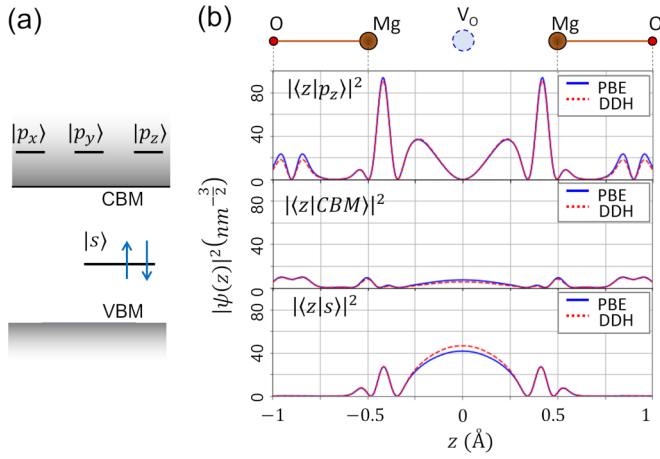


FIG. 2. (a) Schematic representation of the energies of the $|s\rangle$ and $|p\rangle$ states localized at the $V_O: \text{MgO}$ that participate in optical absorption and emission transitions. The conduction band minimum and valence band maximum of the host are indicated by CBM and VBM, respectively. (b) Projections of the square moduli of the Kohn-Sham wave functions $|\psi(z)|^2$ of the $|s\rangle$ and $|p_z\rangle$ states along a chosen direction z , computed with semilocal (PBE) and hybrid (DDH) functionals (Appendix F). Owing to the highly localized nature of the orbitals, the inclusion of the exact exchange in the KS Hamiltonian has little effect on the orbital, as seen by the difference between PBE and DDH results.

III. RESULTS: F CENTER IN MgO

In recent years MgO has been studied as a potential host for spin defects to build quantum memories and quantum networks [68]. In such systems, it is common to observe energy transfer between spin defects acting as quantum emitters and oxygen vacancies present in the surrounding environment, resulting in dephasing of the spin defects. Similarly, in substrates with coexisting rare-earth dopants and oxygen vacancies, NRET from rare earths to the localized states of the oxygen vacancies constitute a possible excitation process. Particularly if such excitation process is dominantly a spin-flip transition, it could be used to create long lived defect excitations.

Here we consider the energy transfer to an F center, i.e., a neutral oxygen vacancy ($V_O: \text{MgO}$), which has two localized electrons. The $V_O: \text{MgO}$ has been experimentally and theoretically studied for several decades using optical absorption, photoluminescence, and electron spin resonance techniques [69–72]. Experimentally, the optical absorption of neutral F centers is found at ~ 5 eV and emission at ~ 2.3 eV and ~ 3 eV [70,71]. As indicated in Figs. 2(a) and 2(b), the relevant single electron orbitals are the localized s -type (a_{1g}) orbitals that are midgap, filled orbitals in the ground state, and the empty triply degenerate localized p -type (t_{1u}) orbitals (referred to as $p_{x,y,z}$) above the conduction band minimum (CBM). An excitation from the many-body ground $^1A_{1g}$ state may result in either excited singlet ($^1T_{1u}$) or triplet ($^3T_{1u}$) states. The ~ 5 eV absorption is assigned to the singlet-to-singlet transition $^1A_{1g} \rightarrow ^1T_{1u}$ [36–38,70,71,73–76] and the singlet-to-triplet absorptions are known to be forbidden at far field. There has been much debate regarding the nature

of the emission [68–70,72–75]. Recent work has shown that the ~ 2.3 eV emission likely originates from the transition from the triplet $^3T_{1u}$ to the ground state $^1A_{1g}$ [37,38], whereas the ~ 3 eV emission is likely from a bound exciton [38]. All studies of optical absorption and emission on the $V_O: \text{MgO}$ reported so far have only addressed the far-field regime, as most studies of point defects in solids. Below we explore the near-field regime.

A. Transition matrix elements as a function of distance at near field

When the distance between the emitters in a host is small compared to the wavelength of the photon being exchanged, the lifetime of the photon is shorter than its time period. The energy of such a short-lived photon (commonly referred to as virtual photon [9]) exhibits a large quantum uncertainty, resulting in an electric and magnetic field that vary as $\sim 1/R^3$ [1], R being the distance from the source (see Fig. 1). As R increases, the photon's propagation characteristic and its lifetime vary [10], eventually leading to an $\sim 1/R$ dependence of the E and H fields at larger distances. For typical atomic defects, the spatial extent of the emitter can be ignored compared to the variation of the field at this far-field regime, leading to the dipole approximation. In contrast, at the near field, the energy density and the E and H fields of the photon may vary significantly over the spatial extent of an absorber, and higher order multipoles cannot be neglected when describing the energy transfer processes [2,12].

We numerically computed the matrix elements $v_{k,\alpha\beta}^{(A)}(\bar{R})$ [Eqs. (10) and (2) with $g = 2$] for an oxygen vacancy in MgO. As discussed earlier, the relevant transition corresponding to optical absorption are between the defect- s and the defect- p orbitals [36–38, details in Appendix D]. For the energy scale of the photon of a few eV, the Frank-Condon principle applies [77,78]. Thus, the orbital wave functions [Fig. 2(b)] are calculated using first-principles DFT calculations (Appendix F) at the ground state relaxed configuration of the ions. As suggested by previous works [36–38], we also neglect the forbidden transition from the defect s orbital to the conduction band minimum. We first verified that the transition between the far-field, $1/R$ and near-field $1/R^3$ regimes occurs, as expected, at $R \sim 1/k$; for the 5-eV optical absorption line this distance corresponds to ~ 20 nm. Separations of < 20 nm can be readily reached at realistic doping concentrations of ~ 10 ppm, indicating that near-field energy transfer is a relevant process in devices. In Figs. 3 (a) and 3(b) we also show the comparison between results obtained with the $\bar{A} \cdot \bar{p}$ and $\bar{E} \cdot \bar{r}$ Hamiltonians for s to p_z type spin conserving transitions ($|GS\rangle \rightarrow |ES\rangle$). Note that, due to the nonlocal nature of the Kohn-Sham Hamiltonian, results obtained with $\bar{A} \cdot \bar{p}$ and $\bar{E} \cdot \bar{r}$ differ. (For comparison with emitter with a local Hamiltonian, see Appendix E).

In $V_O: \text{MgO}$, while the transitions between the GS and the triplet states of the F center are spin forbidden at far field, they have nonzero amplitude at near field, due to the selection rules of the photon emission and absorption when transitions higher than dipolar ones are involved [11]. Hence the sum of the total angular momenta of the electrons in the source and the absorber may not be conserved at near field. Note that by

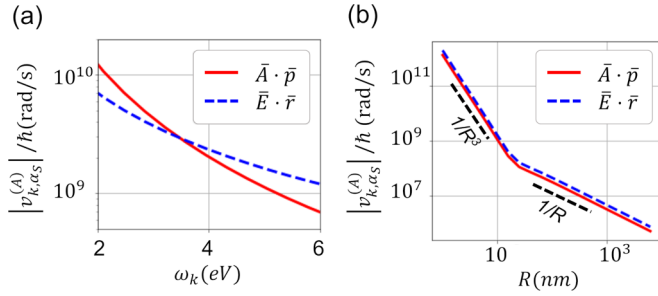


FIG. 3. Comparison between the absorption matrix elements for the ground to excited state singlet transition for $V_O: MgO$ ($v_{k,\alpha_S}^{(A)}$), computed using the $A \cdot p$ Hamiltonian (red curve, see text) and $E \cdot r$ Hamiltonian (blue curve). (a) shows the frequency response at a constant source-to-absorber distance of 10 nm and (b) shows the distance dependence at resonance condition at 5 eV.

the definition, the transition from the GS (singlet) to triplet states could not be studied within a dipolar approximation and/or without considering on the same footing orbital and spin degrees of freedom.

We show in Figs. 4(a) and 4(b) the matrix elements for the GS to singlet and triplet transitions where the near-field source (S) is either of an electric dipole (ED) or magnetic dipole (MD) type. Note, for rare-earth emitters, both the ED and MD type source can naturally exist [7,8]. The case for an ED source ($\alpha_S = \{L = 1, J_z = 0, P = -1\}$) is shown in Fig. 4(a), where the singlet transition is dominant both at near and far field. At near and far field, the matrix element depends on the distance as $\sim 1/R^3$ and $\sim 1/R$ respectively. However, the $|GS\rangle$ to $|^3T_{1u}(m_s = \pm 1)\rangle$ triplet transition is allowed at the near field. In this case the magnetic field produced by the electric dipole source results in a spin-flip transition from the ground level singlet state to the $m_s = \pm 1$ triplet states. To flip the spin along the z axis, one needs to consider the action of the Pauli operators σ_X or σ_Y . Thus the spin-flip processes in the Z basis include contributions by the X and Y components of the magnetic field, i.e., $g \frac{e\hbar}{2m_0} \sigma_X \hat{x} \cdot \vec{\nabla} \times \vec{A}$

and $g \frac{e\hbar}{2m_0} \sigma_Y \hat{y} \cdot \vec{\nabla} \times \vec{A}$ terms of H_{int} of Eq. (2), which explains the observed radial dependence reported in Fig. 4(a). The $|GS\rangle$ to $|^3T_{1u}(m_s = 0)\rangle$ transition remains forbidden even at near field, as the symmetry between the spin up and spin down states is not broken. By including the effect of zero field splitting, or applying an external B field, one can further reduce the symmetry, in which case the $|GS\rangle$ to $|^3T_{1u}(m_s = 0)\rangle$ transition may become active. For example, for a photon state with preferred direction of rotation along a given axis z , the symmetry between the up and down spin is broken and the matrix element for the transition between the singlet and the $m_s = 0$ triplet state becomes nonzero.

The case of a magnetic source is shown in Fig. 4(b). As in Fig. 4(a), the absorber and the source are assumed to lay in the X direction. In this case, the spin flip singlet-to-triplet transition ($|GS\rangle$ to $|^3T_{1u}(m_s = \pm 1)\rangle$) becomes dominant, compared to the spin-conserving singlet-to-singlet ($|GS\rangle$ to $|^1T_{1u}\rangle$) one. Also, the radial dependences are significantly different. The spin nonconserving transitions are dominated by the Y directional magnetic field produced by the magnetic dipole [i.e., the $g \frac{e\hbar}{2m_0} \sigma_Y \hat{y} \cdot \vec{\nabla} \times \vec{A}$ term of the interaction Hamiltonian of Eq. (2)] whereas the spin nonconserving transition are dominated by the action of $\frac{e\vec{A}\cdot\vec{p}_i}{m_0}$. This result highlights the striking difference between far-field and the near-field absorption processes. The spin-flip singlet-to-triplet transition is expected to give rise to a long-lived excited state at the F center and carries great significance towards the proposed optical memory platform (Appendix A), where excitations are transferred from RE emitters to nearby oxygen vacancies. Note that magnetic dipole radiation naturally exists for 4f-4f and 4f-5d transitions in several platforms of rare-earth doped oxide systems [7,8]. Further, the z -directional magnetic dipole source produces a z -directional magnetic field at the absorber, leading to a symmetry breaking between the spin up and down states. This symmetry reduction results in a nonzero absorption matrix element for the ($|GS\rangle$ to $|^3T_{1u}(m_s = 0)\rangle$) transition as shown by the purple curve. Interestingly, at large distances, the spin conserving transition (red curve) becomes dominant again, highlighting the importance of the explicit treatment of

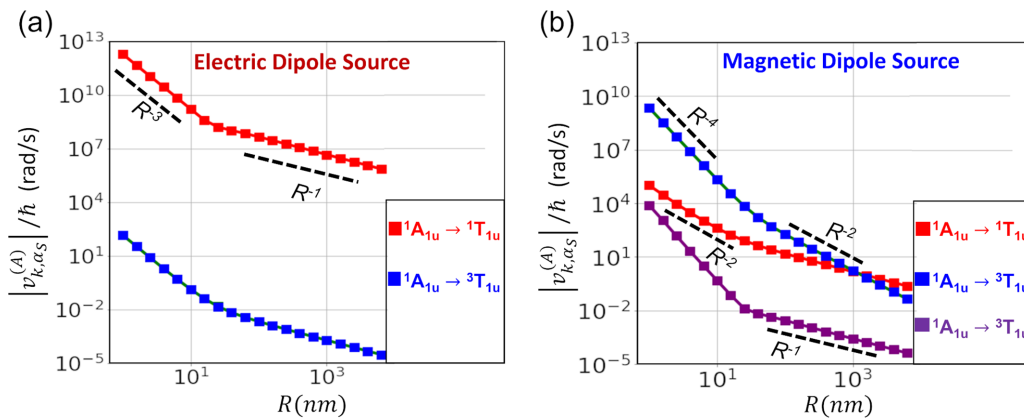


FIG. 4. The distance dependence (R , see Fig. 1) of the matrix element $|v_{k,\alpha_S}^{(A)}(\vec{R})|$ at a fixed direction $\hat{R} = \hat{X}$ for the spin conserving ($^1A_{1u} \rightarrow ^1T_{1u}$; red squares) and spin nonconserving ($^1A_{1u} \rightarrow ^3T_{1u}$; blue and purple squares) absorption transitions in the $V_O: MgO$ center for (a) Electric dipole source and (b) Magnetic dipole source. Blue and purple squares indicate the transition to $^3T_{1u}(m_s = \pm 1)$ and to $^3T_{1u}(m_s = 0)$, respectively. The power law behavior of the matrix elements as a function of R is shown for each matrix element. The results indicate that for energy transfer from a magnetic dipole source, a dominant spin nonconserving transition can be achieved in the near field.

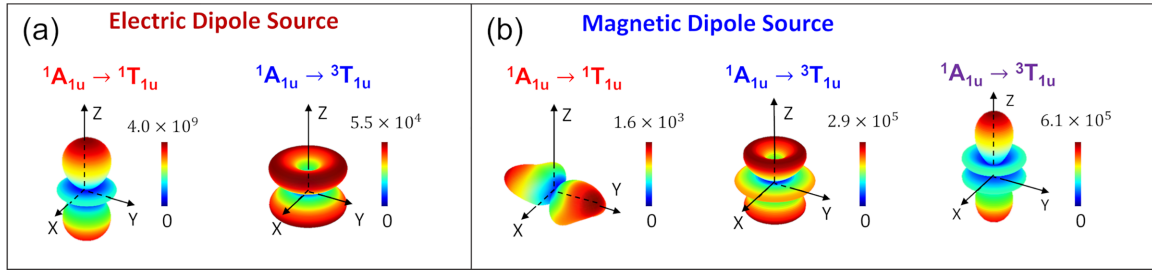


FIG. 5. The angular dependence of the absorption matrix element $|v_{k,\alpha_S}^{(A)}(\vec{R})|$ at a fixed source-absorber distance of $R = 10$ nm for the spin conserving and spin nonconserving absorption transitions in the $V_O: \text{MgO}$ center for (a) Electric dipole source and (b) Magnetic dipole source. The color code for transitions is the same as in Fig. 4. The color scale represents the value of $|v_{k,\alpha_S}^{(A)}|/\hbar$ in the units of rad/s.

the absorption of a photon at the near field, as a function of the distance, as enabled by the framework proposed here. Overall, the results reported in Fig. 4 provide guidance and insight towards singlet-to-triplet absorption processes that may be used for the design of optical memories.

We get further insight into the difference between far and near-field processes by studying the angular distribution of the absorption matrix elements. We fix the source-absorber distance at 10 nm (near field in our case) and vary the source-to-absorber direction \hat{R} . For the ED and MD sources, $|v_{k,\alpha_S}^{(A)}(\vec{R})|$ is plotted as a function of \hat{R} and the resulting angular distributions are shown in Figs. 5(a) and 5(b), respectively, for the spin-conserving ($|GS\rangle$ to $|{}^1T_{1u}\rangle$) and spin nonconserving ($|GS\rangle$ to $|{}^3T_{1u}(m_s = \pm 1)\rangle$) (blue), and ($|GS\rangle$ to $|{}^3T_{1u}(m_s = 0)\rangle$) (purple) transitions. Note that the angular symmetry of the spin-conserving and spin nonconserving transitions are different for ED and MD sources. This difference is interesting as it implies that at certain specific orientations between the source and the absorber, spin nonconserving processes can be engineered to become dominant; hence our results provide insight into geometrical configurations which may be attained by nanofabrication design to control the angular orientation between the source and absorber.

We further explore $v_{k,\alpha_S}^{(A)}(R, \theta)$ for ED and MD transitions in Fig. 6. Figure 6(a) shows a two-dimensional plot for $v_{k,\alpha_S}^{(A)}(R, \theta)$ for the $|GS\rangle$ to $|{}^1T_{1u}\rangle$ transition by an electric dipolar mode ($\alpha_S = \{L, J_z, P = 1, 0, -1\} = ED$) as a function of the distance R and the polar angle θ of the source at which the absorber sits. In Fig. 6(b) we plot $-\partial(\log|v_{k,\alpha_S}^{(A)}|)/\partial\log R$ for the same transition, which results in the dominant exponent n corresponding to the $|v_{k,\alpha_S}^{(A)}| \sim 1/R^n$ relation. The dashed lines are guides to the eye. At the polar direction ($\theta = 0$ and π , $\pm Z$ direction), the associated fields are zero and the matrix element is only a result of the field gradient across the finite size of the absorber, thus the radial dependence is $\sim 1/R^2$ even at far field. In contrast, near the equator, ($\theta = \pi/2$, XY plane), a standard near field to far-field transition of $\sim 1/R^3$ to $\sim 1/R$ behavior is observed for $|v_{k,\alpha_S}^{(A)}|$.

In Figs. 6(c) and 6(d), we show the results for a MD source inducing a spin nonconserving $|GS\rangle$ to $|{}^3T_{1u}(m_s = \pm 1)\rangle$ transition. These results are markedly different from those obtained in the ED case. Now, the equator ($\theta \sim \pi/2$) is the zone where the B field at the equatorial plane has only a z component. Thus, the gradient of the B field results in the nonzero

part of the matrix element and hence the radial dependence, even at $R > 10$ nm, is $\sim 1/R^2$.

The results shown in Figs. 4–6 map out the distance and angle dependence for the near-field matrix elements pertaining to energy transfer processes, and involving spin allowed and spin forbidden transitions for both electric and magnetic dipolelike sources. Our findings indicate that the symmetry of the angular distribution of the matrix elements corresponding to spin conserving and nonconserving transitions are different; hence our calculations point at possible design rules for geometrical configurations more prone to yield long-lived transitions useful to create desired states of memories or quantum networks in solid hosts.

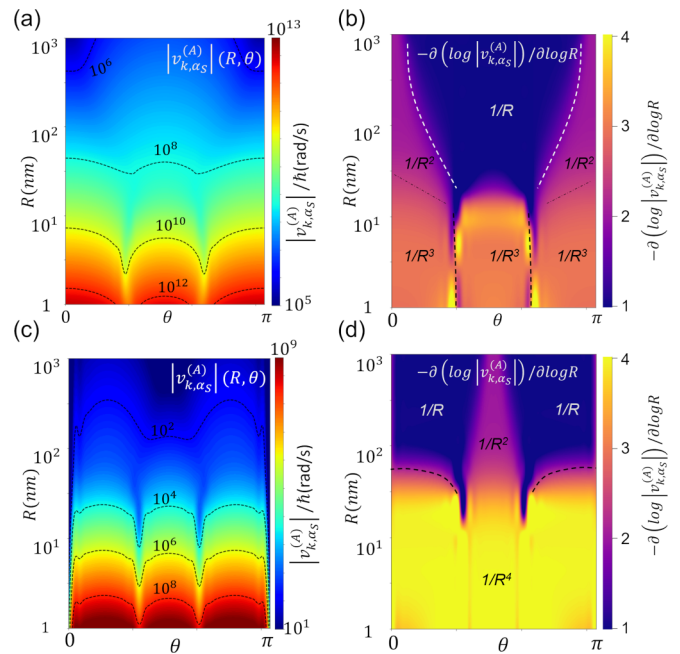


FIG. 6. The distribution of photon absorption matrix element $|v_{k,\alpha_S}^{(A)}(\vec{R})|$ for (a) spin conserving $|GS\rangle$ to $|{}^1T_{1u}\rangle$ and (c) spin nonconserving $|GS\rangle$ to $|{}^3T_{1u}(m_s = \pm 1)\rangle$ transitions showing the response as a function of source-absorber distance R , and the polar angle θ (For these cases, cylindrical symmetry (Fig. 5) ensures no variation with ϕ). (b) and (d) show the plots of exponent n of the $\sim 1/R^n$ dependence of $|v_{k,\alpha_S}^{(A)}|$ ($n = -\partial(\log|v_{k,\alpha_S}^{(A)}|)/\partial\log R$). The dashed lines in (b) and (d) are guide to the eye to indicate the boundary where the exponent n changes its value.

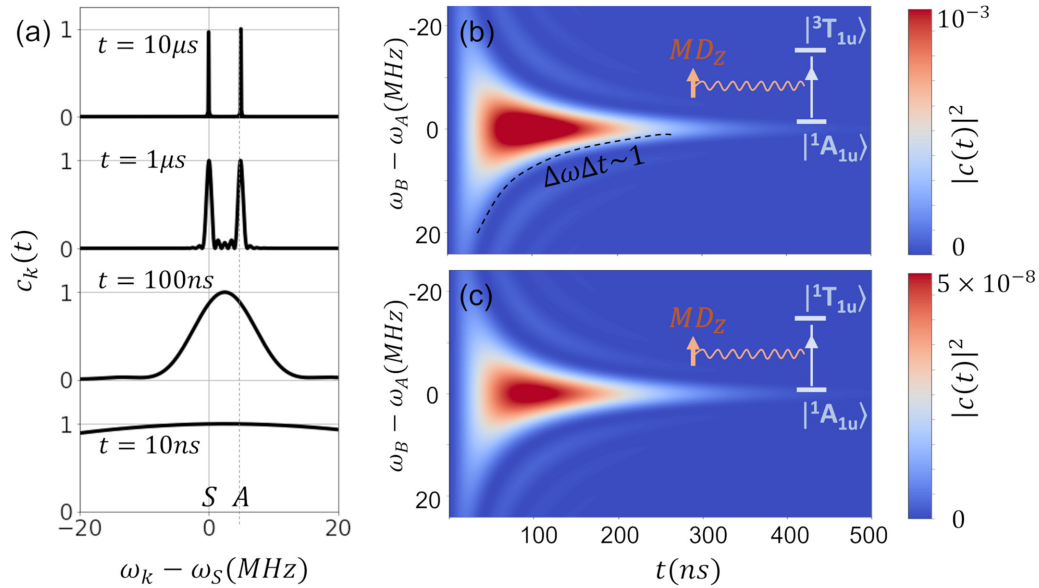


FIG. 7. (a) Normalized spectrum of the photon amplitude $c_k(t)$ as a function of the photon frequency (ω_k) at different times = 10 ns, 100 ns, 1 us, and 10 us for the energy difference between source and absorber transition $\omega_A - \omega_S = 5\text{MHz}$. (b) Two-dimensional plot of the NRET probability ($|c(t)|^2$) as a function of time and frequency mismatch $\omega_A - \omega_S$ for a magnetic dipole source (MD) of oscillator strength 1, which induces a singlet-to-triplet transition. The corresponding singlet-to-singlet transition for the same MD source is shown in (c) which is much weaker compared to the singlet-to-singlet transition at this configuration.

B. Transfer rate calculations

We now turn to examining the NRET transfer rate. We consider a physical source of unity oscillator strength, which is a realistic oscillator strength for deep-levels such as rare-earth centers [8]. For a generic source of oscillator strength f_{osc} the emission matrix elements satisfy

$$\sum_{\alpha_S} |v_{k,\alpha_S}^{(S)}|^2 = \left(\frac{\mu_0 \hbar^2 \omega_k^2 e^2}{3\pi^2 m_0} \right) f_{\text{osc}}. \quad (14)$$

Here μ_0 represents the vacuum permeability. Equation (14) yields the emission matrix element of a generic source if the energy ω_k and the oscillator strength are known.

With the knowledge on the specific type of a multipole source (α_S specified), Eq. (14) can be used to calculate the emission matrix element values up to an arbitrary phase. Here we show the transfer amplitude for purely electric dipole source with $\alpha_S = \{\text{L}, \text{J}_z, \text{P} = 1, 0, -1\}$, and a purely magnetic dipole source with $\alpha_S = \{\text{L}, \text{J}_z, \text{P} = 1, 0, 1\}$. We assume in each case that all the other multipole components vanish. Thus, from Eq. (14) we have $|v_{k,\alpha_S}^{(S)}| = \sqrt{\left(\frac{\mu_0 \hbar^2 \omega_k^2 e^2}{3\pi^2 m_0} \right) f_{\text{osc}}}$, where α_S is either $\{\text{L}, \text{J}_z, \text{P} = 1, 0, -1\}$, or $\{\text{L}, \text{J}_z, \text{P} = 1, 0, 1\}$ corresponding to electric or magnetic dipoles, respectively. The unknown phase of $v_{k,\alpha_S}^{(S)}$ factors out as a global phase in calculation of the NRET matrix element as per Eq. (12). Also note that here for simplicity we have assumed the source to be an ideal dipole. For a realistic defect as the source, $v_{k,\alpha_S}^{(S)}$, the emission matrix elements can be readily computed from first principles as shown in Eqs. (11), and (14) can then be used to estimate the oscillator strength of the source.

We consider short time scale processes for which there can be finite transfer even for a finite energy mismatch. At

small time, $\Delta\omega\Delta t \ll 1$, the width of the spectrum of $c_k(t)$ [Eq. (13)] is relatively large and it gradually decreases as t increases. This is shown in Fig. 7(a) for the spin nonconserving $|GS\rangle$ to $|^3T_{1u}(m_s = \pm 1)\rangle$ transition, induced by a magnetic dipole source of oscillator strength 1. The corresponding NRET probability of coherent transfer is shown in Fig. 7(b) as a function of both time in the horizontal axis and the energy mismatch between the source and the absorber in the vertical axis. As a comparison we also show in Fig. 7(c) the transfer probability for the spin-conserving singlet-singlet transition for the same magnetic dipole source of 1 oscillator strength. While the energy-time uncertainty behavior in Fig. 7(c) is the same as in Fig. 7(b), the transfer amplitude is negligible compared to that of the spin nonconserving transition. This is an interesting example of the spin nonconserving transition dominating over the spin conserving one for a realistic near-field process.

C. Effective parameter to characterize coherent transfer

Historically, the energy transfer between emitters has been characterized using the notion of the Förster radius [1]. Such radius is defined as the distance between a source and an absorber at which the energy transfer rate between the source and the absorber matches the rate of radiative decay of an isolated source, resulting in a 50% probability of the transfer. In most systems investigated in the chemistry literature, the energy transfer of interest is between a large number of sources and absorbers. Thus, averaging over angular coordinates has been always implicit. However, in the solid state, using thin film growth, nanofabrication, and spatially selective doping techniques, some control can be achieved on the relative placement of the source and the absorber sites. Thus, the angular dependence cannot be assumed to be averaged out.

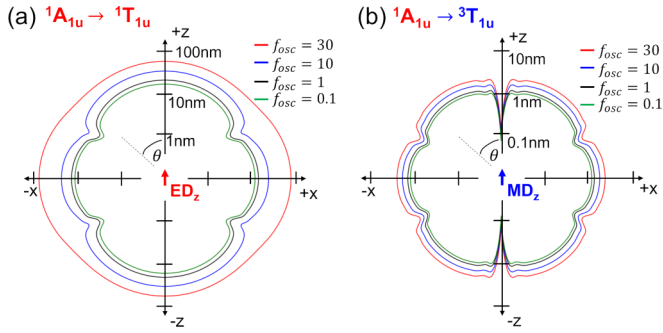


FIG. 8. Contour plots of the parameter R_{eff} (see text) for the (a) singlet-singlet absorption transition by an F center from an electric dipole source, at near field, and the (b) singlet-to-triplet absorption from a magnetic dipole source. The different lines indicate cases with different oscillator strengths of the dipolar source: $f_{\text{osc}} \sim 0.1$ to 1 represents a deep-level source whereas, $f_{\text{osc}} \sim 10$ to 30 represents larger sources like quantum dots.

Note that due to the large phonon induced broadening in room temperature measurements in solution chemistry and biological systems, the emission and absorption spectra are always incoherently broad, resulting in a dominant incoherent energy transfer. Our interest lies in a different regime and pertains to solid state environments. First, several deep-level systems such as rare-earth substitutional sites, NV centers, and other point defects, exhibit narrow emission spectra compared to the measurement time scale. Second, in the solid state most characterizations and device design occur at cryogenic temperature which suppresses decoherence and dephasing and can lead to even $< \text{kHz}$ linewidths [7,8]. Thus, in the following, we define a parameter representing the equivalent of a Forster radius for angle resolved configurations, but for coherent processes, and we include spin conserving and non-conserving transitions in the coherent limit.

We define the effective radius R_{eff} as a function of the direction defined by the unit vector $\hat{R} = (\theta, \phi)$ from the source S to the absorber A such that $\max(|c(t)|^2) = 1/2$. Using Eq. (7) we get $|c(t)|^2 = \frac{4M^2}{\hbar^2} \frac{\sin^2(\Delta\omega t/2)}{\Delta\omega^2} e^{-t/T_{1S}}$. Here T_{1S} is the average time for the source to emit a single photon and can be estimated directly from the oscillator strength as $T_{1S} = \frac{6\pi\epsilon_0 m_0 c^3}{f_{\text{osc}} n_i \omega^2 \rho^2}$. The maximum probability is achieved at $t = t_{\text{max}} = 2 \frac{\text{atan}(\Delta\omega T_{1S})}{\Delta\omega}$. Imposing $|c(t)|^2|_{t=t_{\text{max}}} = \frac{1}{2}$, and invoking $M = \frac{i\pi n_i}{\hbar c} \sum_{\alpha} v_{k_S, \alpha_S}^{(S)} v_{k_S, \alpha_S}^{(A)}$ we get

$$\frac{\pi^2 n_i^2}{\hbar^2 c^2} \left| \sum_{\alpha} v_{k_S, \alpha_S}^{(S)} (R_{\text{eff}}, \hat{R}) v_{k_S, \alpha_S}^{(A)} \right|^2 = \frac{\hbar^2 (1 + T_{1S}^2 \Delta\omega^2)}{8T_{1S}^2} e^{\frac{t_{\text{max}}}{T_{1S}}}. \quad (15)$$

Solving Eq. (15) numerically for an arbitrary source and arbitrary absorber yields R_{eff} as a function of the source-to-absorber direction \hat{R} .

We show R_{eff} at resonant conditions ($\Delta\omega = 0$) for (1) the singlet ($|GS\rangle$) to singlet ($|^1T_{1u}\rangle$) absorption for a near-field electric dipole source, and (2) the singlet ($|GS\rangle$) to triplet ($|^3T_{1u}(m_s = \pm 1)\rangle$) absorption for a near-field magnetic dipole source in Figs. 8(a) and 8(b), respectively. The function $R_{\text{eff}}(\theta)$ is shown as a polar plot in the XZ plane—but a

rotational symmetry around the Z axis can be assumed. The different lines in Figs. 8(a) and 8(b) represent different values of the oscillator strength of the source dipole, encompassing a vast category of emitters including deep levels ($f_{\text{osc}} \sim 0.1$ to 1) and quantum dots ($f_{\text{osc}} \sim 10$ to 30). We find that for the spin conserving transition from an ED source of $f_{\text{osc}} = 1$, $R_{\text{eff}} \approx 10$ nm whereas for the spin nonconserving transition from a MD source, $R_{\text{eff}} \approx 2$ nm. Distances of ~ 2 –10 nm are realistic distances in either random ensembles or controlled pairs of defects and emitters in semiconductors and insulators. Additionally, with increasing $\Delta\omega$, as per Eq. (15) the variation of the matrix element follows approximately a Lorentzian and the R_{eff} drops accordingly. We see from Fig. 8 that in several cases, for both ED and MD sources, an angular coarse graining may not be appropriate as there is a high degree of variation of R_{eff} as a function of the source-absorber polar angle θ . These results provide a possible way to understand quantitatively how to guide the growth and nanostructuring of a solid host to facilitate specific, desired transitions.

IV. DISCUSSION

We investigated the transfer of energy between localized emitters in a solid and explored the spin nonconserving transitions in the near field. In most realistic materials and devices for quantum information and classical optical applications, native or implanted defects reside at distances at which near-field energy transfer occurs. In some case near-field transfer may be undesirable (e.g., in some quantum information applications [7] where specific transitions of a given defect are of interest for optical addressability); in some other cases, near-field transfer can represent an opportunity to design new functionalities. The investigation of the new functionality proposed here (ultradense classical memories) requires an approach beyond the dipole approximation, where orbital and spin degrees of freedom are considered on the same footing and the interactions between emitters and the solid matrix are taken into account. The perturbative approach presented in this paper includes first-principles calculations of electronic states and accounts for the quantum nature of the broad spectrum virtual photons mediating the energy transfer. Our findings indicate that for realistic oxides, magnetic and spin nonconserving transitions are key to understanding light-matter interaction and to derive design rules to engineer long-lived transitions. The approach provides a way to address a wide variety of NRET processes that are highly relevant to quantum and classical optical devices—specifically optical memories, quantum optical networks, and quantum memories.

Specifically, we applied our approach to the F center in MgO, and we presented a systematic study of the NRET amplitude for spin-conserving (singlet-to-singlet) and spin nonconserving (singlet-to-triplet) absorption transitions originating from a near-field source (e.g., a RE impurity) of magnetic or electric dipole type, as a function of the relative orientation and distance between the source and the absorber. We showed that in certain configurations of the source and the absorber, singlet-to-triplet transitions not only become active at near field but constitute the dominant process. Our study revealed some key design principles to realize such singlet-to-

triplet type transitions at the near field. In the case of the F center in MgO we found that a magnetic dipole type source is necessary to obtain dominant spin nonconserving transitions. In the case of rare-earth-doped oxides, an intrinsic magnetic dipole type emission is available [7,8], thus providing a viable path to create long-lived excited state in localized defects that are relevant to rare-earth based ultrahigh density optical memory platforms envisioned in this work (Appendix A). Our approach can be used to facilitate material search to identify spectrally matched rare-earth-defect combinations for such optical memory platforms.

We also explored the NRET amplitude as a function of the angle between the source and the absorber and shown a significant angular variation of both the amplitudes and the radial dependence of the absorption matrix elements of the transitions. This variation represents a significant result as it provides insight into nanofabrication design where certain processes may be favored by engineering specific geometrical configurations of the emitters. Finally, we found that the effective radius for singlet-to-triplet transition in V_O : MgO is ~ 1 – 2 nm for coherent transfer rate of 50% of the radiative decay, which provide insight into the required density of the source and absorber site in the host material to enable such processes.

Importantly, although we showed results for an exemplar oxide, V_O : MgO, the approach presented here is general and applicable to any localized defects in any solid that can be described using first-principles calculations. In addition, our approach is easily generalizable to distributed systems of defects thus allowing for the study of near-field energy transfer in larger emitters such as quantum dots, as well as defects and dopants with inhomogeneous distributed spectral lines. These include the interaction between different REs for quantum memories, the interaction between a localized defect acting as a quantum memory with another localized defect acting as a qubit, and energy trapping by localized electronic states.

In the results presented here we have assumed a uniform and isotropic medium for simplicity. However, the host material may often exhibit an anisotropic dielectric response. In addition, in most practical applications, the host can be in the form of a membrane/film. Under those circumstances, Eq. (8) still holds, but the spherical harmonics are no longer the eigenfunctions of the Maxwell equations, and thus the propagating photon in a specific multipole mode α_S may scatter to a different multipole mode α'_S due to the medium. This effect can be readily accounted for by explicitly including the photon Green function expressed in the multipole basis between the source and the absorber, resulting in a revised Eq. (12) as $M = \frac{i\pi n_i}{\hbar c} \sum_{\alpha_S, \alpha'_S} v_{k_S, \alpha_S}^{(S)} G_{\alpha_S, \alpha'_S}(\vec{r}_S, \vec{r}_A) v_{k_S, \alpha'_S}^{(A)}$.

Thus, the framework reported here is readily generalizable to anisotropic media.

Our approach is suited for addressing photon hopping in large ($\sim \mu\text{m}$) ensembles, taking into account finite energy uncertainty, and including spin flip and spin conserving processes alike. The computational cost of the method presented here is only limited by the computation of the matrix elements at the separate localized emitters and thus large-scale systems with emitter-emitter distances ranging from ~ 1 to ~ 1000 nm can be tackled with equal computational cost.

Furthermore, using the first-principles electronic structure calculation paves the way to include lattice relaxation between energy transfer processes in a chain of emitters. The excited states of many localized emitters of interest undergo significant relaxation compared to the ground state. The approach reported here provides a pathway to understanding such physics of collective emitters in realistic devices towards classical and quantum photonic applications.

ACKNOWLEDGMENTS

We thank Prof. J. Sofo, Dr. Y. Jin, and Dr. C. Vorwerk for useful discussions. We acknowledge the computational resources of the National Energy Research Scientific Computing Center (NERSC), a DOE Office of Science User Facility supported by the Office of Science of the U.S. Department of Energy under Contract No. DE-AC02-05CH11231, and the computational resources of the University of Chicago Research Computing Center (RCC). This work was supported by the U.S. Department of Energy, Office of Science, for support of microelectronics research, under Contract No. DE-AC0206CH11357.

APPENDIX A: NEAR-FIELD ENERGY TRANSFER IN ULTRAHIGH DENSITY OPTICAL MEMORY

In this section we discuss the key concept behind a potential platform of ultrahigh density optical memories with RE emitters and defects in oxides, a platform where the near-field energy transfer plays a critical role. The approach exploits 4f-4f transitions of rare-earths that lead to very narrow linewidth (sub kHz) even in solid state, with the typical inhomogeneous spread of these transitions being of \sim MHz to \sim GHz range [7,8]. The large inhomogeneous spread relative to the narrow homogeneous linewidth provides a way to optically address a large number ($\gtrsim 1000$) of RE atoms even within a diffraction limited volume and provides a potential path to ultrahigh density optical memories.

However, the lifetime of the optically excited state is still limited by the radiative decay lifetime of the RE emitters (typically ~ 10 ms). We propose that a possible route to enhance the lifetime is to transfer the excitation to a proximal defect. Further, by inducing transitions that are spin nonconserving, i.e., optically forbidden in the far field, one can potentially create longer lifetimes.

The basic idea is captured in Fig. 9. Each cell in the left panel represents an optically addressable memory cell doped with RE emitters (red) and suitable defects (blue) that exhibit optical absorption transitions in the same band at the RE emission. Individual RE ions can be identified by their narrow spectral lines and optically excited. The excitation can then be transferred and trapped into a nearby defect (e.g., an oxygen vacancy in an oxide). For typical doping concentration of \sim few ppm, the average REs and vacancies can reach ~ 5 to ~ 10 nm, a distance much smaller than the wavelength of the optical/near IR photons (~ 500 nm to $\sim 1 \mu\text{m}$). Thus, understanding near-field energy transfer is critical to understand the transfer process. Further, the excitation of the trap could be quenched, or Stark shifts could be exploited in the RE emission process as readout mechanisms.

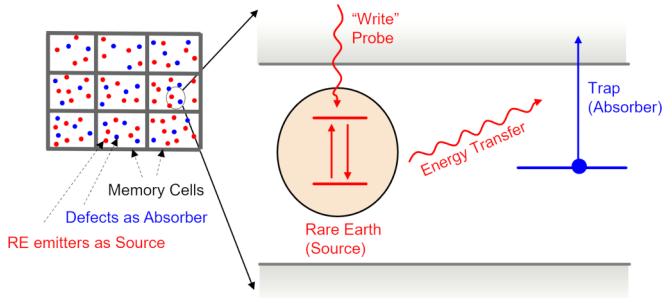


FIG. 9. A schematic representation of ultrahigh density optical memories where each memory-cell in a solid host (left panel) contains an ensemble of RE emitters (red) and point-defects (blue). Right: A RE emitter-defect complex representing the working “unit” of the memory. Optical excitations of RE emitters that are spectrally separated can be transferred to a suitable defect in the proximity of the emitter to trap the excitation and increase its lifetime (see text).

Understanding the design rules required to engineer the processes described above call for (1) exploring possible combinations of RE emitters, defects, and host oxides to allow spectrally matched RE-defect combinations, and (2) a quantitative understanding of the energy transfer rates for optically allowed and optically forbidden absorption transitions in the near field and (3) understanding the energy trapping and relaxation dynamics. The combination of (1), (2), and (3) demands a unified approach between first-principles electronic structure calculations and quantum electrodynamical near-field energy transfer in the solid state, which is the framework established in this work.

APPENDIX B: MULTIPOLE BASIS OF THE PHOTON

We used a multipole basis to represent photon modes [55,56,57] in a uniform dielectric medium; this basis facilitates investigating the transfer/ conservation of angular momentum states during the energy transfer process [11] as all the multipole modes are eigenfunctions of the angular momentum operator. In this section we give a brief overview of how we represent photon modes.

In Fig. 10 we consider a spherical cavity of radius R_{norm} centered around the source denoted as S, here taken as a two-level system. The ladder-down operator of this two-level system is $\hat{\sigma}_S$ and \hat{a}_{k, α_S} represents the annihilation operator of a photon mode with radial wavevector k and $\alpha_S = \{L, J_Z, P\}$ in the spherical cavity. Here L denotes the orbital angular momentum of the photon, J_Z is the total (orbital + spin) angular momentum, and P the parity. The multipole basis provides a complete orthogonal basis of the cavity photon mode and can be appropriately normalized for finite R as shown below. We then consider another two-level system, denoted as A, that acts as the absorber and has $\hat{\sigma}_A$ as the operator representing annihilation of an excitation.

We can rewrite the overall Hamiltonian of the interacting source-absorber system [Eq. (2)] in the second quantized

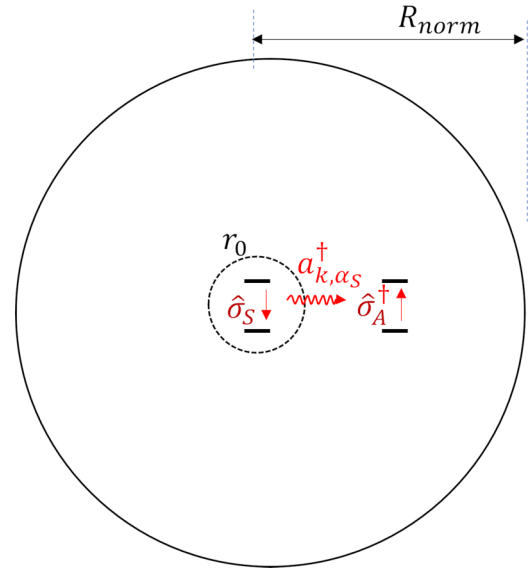


FIG. 10. Schematic representation of the macroscopic system considered in our work, where the photon modes are defined within a sphere of radius R_{norm} centered at the emitter S. The absorber is denoted as A. The photon multipole modes are the propagating photon modes in a multipole basis.

notation as

$$\begin{aligned}
 H = & \omega_S \hat{\sigma}_S^\dagger \hat{\sigma}_S + \omega_A \hat{\sigma}_A^\dagger \hat{\sigma}_A + \sum_{k, \alpha_S} \omega_k \hat{a}_{k, \alpha_S}^\dagger \hat{a}_{k, \alpha_S} \\
 & + \sum_{k, \alpha_S} (\hat{\sigma}_S + \hat{\sigma}_S^\dagger) (V_{k, \alpha_S}^{(S)} \hat{a}_{k, \alpha_S}^\dagger + V_{k, \alpha_S}^{(S)\dagger} \hat{a}_{k, \alpha_S}) \\
 & + \sum_{k, \alpha_S} (\hat{\sigma}_A + \hat{\sigma}_A^\dagger) (V_{k, \alpha_S}^{(A)} \hat{a}_{k, \alpha_S} + V_{k, \alpha_S}^{(A)\dagger} \hat{a}_{k, \alpha_S}^\dagger). \quad (\text{B1})
 \end{aligned}$$

The multipole photon modes [56], i.e., $|1_{k, \alpha_S}\rangle = \hat{a}_{k, \alpha_S}^\dagger |0\rangle$ are a complete basis that can be obtained by solving the Maxwell equations under the boundary condition chosen for a specific problem. The expressions for their vector and scalar potential fields have been defined in Eqs. (3)–(6). R_{norm} shown in Fig. 10 is the radius of the normalizing sphere for the multipole modes which translates to the width of the modes in k space: $\Delta k = \frac{\pi}{R_{\text{norm}}}$. It is apparent from Eqs. (3)–(6) that the vector and scalar potentials of the photons are normalized by $\sqrt{\Delta k}$. The normalization constant is included in $V_{k, \alpha_S}^{(S)}$ and $V_{k, \alpha_S}^{(A)}$. We thus define $V_{k, \alpha_S}^{(S)} = v_{k, \alpha_S}^{(S)} \sqrt{\Delta k}$, and $V_{k, \alpha_S}^{(A)} = v_{k, \alpha_S}^{(A)} \sqrt{\Delta k}$. This definition facilitates the k -space summation over all virtual photons as shown below.

Closed versus open systems. As mentioned above, the photon modes $|1_{k, \alpha_S}\rangle$ are solutions of the Maxwell equation under properly chosen boundary conditions. In the case of perfectly reflecting boundary, e.g., a perfectly enclosing spherical mirror of radius R_{norm} , the radial functions are the Bessel function of type j - resulting in standing wave-type modes of a nondecaying photon. The Bessel j radial dependence can be decomposed into Hankel functions of type 1 and type 2- representing the radially inward propagating and outward propagating waves using the relation: $j_L(kr) = \frac{1}{2}(h_L^{(1)}(kr) + h_L^{(2)}(kr))$ [56,57].

If the boundary of the system is open, the radially outward propagating waves are represented by Hankel function of type 1. In this case, $g_L(kr) = 4\pi i^L h_L^{(1)}(kr)$. Such functions possess a singularity at the origin (phase center). However, this singularity does not affect the evaluation of the emission matrix elements. Thus, we can express the photon mode close to the center ($r < r_0$, for some r_0) by the Bessel j function. Hence for an open system, the photon mode $|1_{k,\alpha_S}\rangle$ represents the radially outward propagating wave, with type 1 Hankel function being the radial function in the source-free region ($r > r_0$), and the Bessel j -type radial function near the source at $r < r_0$ [56].

From Eq. (B1), we rewrite the interaction part of the Hamiltonian as

$$H_{\text{int}} = \left(\sum_{k,\alpha_S} V_{k,\alpha_S}^{(S)} \hat{\sigma}_S \hat{a}_{k,\alpha_S}^\dagger + \sum_{k,\alpha_S} V_{k,\alpha_S}^{(A)} \hat{\sigma}_A^\dagger \hat{a}_{k,\alpha_S} \right) + \text{h.c.} \\ + \left(\sum_{k,\alpha_S} V_{k,\alpha_S}^{(S)} \hat{\sigma}_S \hat{a}_{k,\alpha_S} + \sum_{k,\alpha_S} V_{k,\alpha_S}^{(A)} \hat{\sigma}_A^\dagger \hat{a}_{k,\alpha_S}^\dagger \right) + \text{h.c.} \quad (\text{B2})$$

Here $V_{k,\alpha_S}^{(S)}$ and $V_{k,\alpha_S}^{(A)}$ are the matrix elements corresponding to the photon emission and photon absorption at S and A, respectively, that we evaluate in the main text.

APPENDIX C: DESCRIPTION OF THE ELECTRON STATES

The source S and the absorber A may possess generic many-electron states; in general we have $H_X|\Phi^{(X)}\rangle = E^{(X)}|\Phi^{(X)}\rangle$ where $X = S, A$. The many electron eigenstates $|\Phi^{(X)}\rangle$ can be represented by a sum of Slater determinants constructed from single electronic states $\{|\phi_i^{(X)}\rangle, i = 1 : N_X\}$ where N_X is the number of the single particle electronic states in emitter X. The Hamiltonians H_S and H_A may be approximated by the Kohn-Sham Hamiltonian in density functional theory [28–30], or with effective Hamiltonians derived from a chosen active space using, e.g., using quantum embedding theories [34–37], depending on the level of electronic structure theory needed. The ground state of S or A can be generically represented as

$$|GS^{(S/A)}\rangle = \sum_{\substack{i \in \text{occ} \\ j \in \text{unocc}}} \alpha_{ij}^{(GS)} c_j^{(S/A)\dagger} c_i^{(S/A)} |D^{(S/A)}\rangle, \quad (\text{C1})$$

and similarly, the excited state

$$|ES^{(S/A)}\rangle = \sum_{\substack{i \in \text{occ} \\ j \in \text{unocc}}} \alpha_{ij}^{(ES)} c_j^{(S/A)\dagger} c_i^{(S/A)} |D^{(S/A)}\rangle, \quad (\text{C2})$$

where $|D^{(S/A)}\rangle$ represents the Slater determinant built from the first filled N orbitals, i.e., $|D^{(S/A)}\rangle = \prod_{i=1}^N c_i^{(S/A)\dagger} |0\rangle$. Here $c_i^{(S/A)}$ denotes the annihilation operator of an electron in the single electronic state $|\phi_i^{(S/A)}\rangle$. Note that Eqs. (C1) and (C2) represent the generic form in which the many body electron states are represented and the orbitals and the α coefficients are determined from the electronic structure calculations.

APPENDIX D: MATRIX ELEMENTS FOR OPTICALLY ALLOWED AND FORBIDDEN TRANSITIONS IN V_0 : MGO

The matrix elements for transitions from a many-body ground to an excited state can be obtained by adding up all possible single-orbital matrix elements based on the Slater-Condon rule. For a transition from any generic many-body state $|\Phi\rangle$ to the state $|\Phi_1\rangle = c_j^\dagger c_i |\Phi\rangle$, we have

$$\langle \Phi_1 | \hat{O} | \Phi \rangle = \langle \phi_j | \hat{O} | \phi_i \rangle = O_{ji}. \quad (\text{D1})$$

Thus, for a generic single excited state: $|ES^{(A)}\rangle = \sum_{\substack{i \in \text{occ} \\ j \in \text{unocc}}} \alpha_{ij} c_j^{(A)\dagger} c_i^{(A)} |GS^{(A)}\rangle$, we have

$$\langle ES^{(A)} | \tilde{H}_{\text{int}} | GS^{(A)}, 1_{k,\alpha_S} \rangle = \sum_{\substack{i \in \text{occ} \\ j \in \text{unocc}}} \alpha_{ij}^* \langle \phi_j^{(A)} | \tilde{H}_{\text{int}} | \phi_i^{(A)}, 1_{k,\alpha_S} \rangle. \quad (\text{D2})$$

For the V_0 : MgO center, we use Eq. (D2) to write the matrix elements for the optical absorption singlet-to-singlet and singlet-to-triplet transitions below. The electronic defect states are localized midgap s-type orbital ($|s\rangle$) and localized p-type orbitals ($|p_x\rangle, |p_y\rangle, |p_z\rangle$) just above the conduction band edge. In the ground state configuration of the neutral F center, both spin states of the s orbitals are filled resulting in a singlet ground state $|GS\rangle = |s_\uparrow, s_\downarrow\rangle$. Here $|s_\uparrow, s_\downarrow\rangle$ represents the Slater determinant where two electrons occupy the defect-s orbital and all valence orbitals are filled. For an excitation to the p_z orbital, the excited singlet can be written as $|^1T_{1u}\rangle = [\frac{1}{\sqrt{2}} \hat{c}_{p_z\uparrow}^\dagger \hat{c}_{s\uparrow} + \frac{1}{\sqrt{2}} \hat{c}_{p_z\downarrow}^\dagger \hat{c}_{s\downarrow}] |s_\uparrow, s_\downarrow\rangle$, or $|^1T_{1u}\rangle = \frac{1}{\sqrt{2}}(|p_{z\uparrow}, s_\downarrow\rangle + |s_\uparrow, p_{z\downarrow}\rangle)$, whereas the three triplet states are $|^3T_{1u}(m_s = 0)\rangle = \frac{1}{\sqrt{2}}(|p_{z\uparrow}, s_\downarrow\rangle - |s_\uparrow, p_{z\downarrow}\rangle)$, $|^3T_{1u}(m_s = 1)\rangle = |s_\uparrow, p_{z\uparrow}\rangle$, and $|^3T_{1u}(m_s = -1)\rangle = |p_{z\downarrow}, s_\downarrow\rangle$. The matrix elements between these Slater determinants can be reduced to the matrix elements between the single electron orbitals in the following way:

$$\langle ^1T_{1u} | H_{\text{int}} | GS, 1_{k\alpha_S} \rangle = \frac{1}{\sqrt{2}} \langle p_{z\uparrow} | H_{\text{int}} | s_\uparrow, 1_{k\alpha_S} \rangle \\ + \frac{1}{\sqrt{2}} \langle p_{z\downarrow} | H_{\text{int}} | s_\downarrow, 1_{k\alpha_S} \rangle, \quad (\text{D3})$$

$$\langle ^3T_{1u}(m_s = 1) | H_{\text{int}} | GS, 1_{k\alpha_S} \rangle = \langle p_{z\uparrow} | H_{\text{int}} | s_\downarrow, 1_{k\alpha_S} \rangle, \quad (\text{D4})$$

$$\langle ^3T_{1u}(m_s = -1) | H_{\text{int}} | GS, 1_{k\alpha_S} \rangle = \langle p_{z\downarrow} | H_{\text{int}} | s_\uparrow, 1_{k\alpha_S} \rangle, \quad (\text{D5})$$

$$\langle ^3T_{1u}(m_s = 0) | H_{\text{int}} | GS, 1_{k\alpha_S} \rangle = \frac{1}{\sqrt{2}} \langle p_{z\uparrow} | H_{\text{int}} | s_\uparrow, 1_{k\alpha_S} \rangle \\ - \frac{1}{\sqrt{2}} \langle p_{z\downarrow} | H_{\text{int}} | s_\downarrow, 1_{k\alpha_S} \rangle, \quad (\text{D6})$$

Note that the ± 1 spin triplet state transitions are spin forbidden at far field, but they can have nonzero contributions at near field. The $m_s = 0$ triplet state transition vanishes if the symmetry between the up and down spin states is not broken. However, for a photon state with preferred direction of rotation along z, the symmetry between the up and down

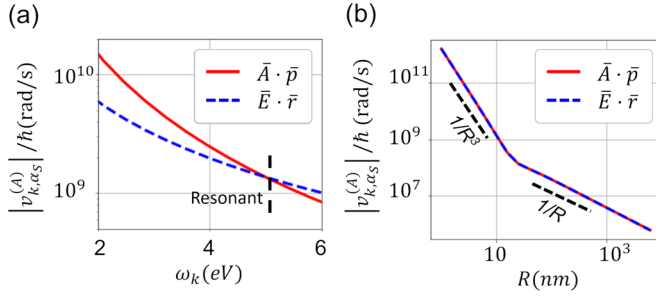


FIG. 11. Comparison between the absorption matrix element ($v_{k,\alpha_S}^{(A)}$) computed using the $A \cdot p$ Hamiltonian (red curve) and $E \cdot r$ Hamiltonian (blue curve) for the $|\phi_{0,0,0}\rangle$ to $|\phi_{0,0,1}\rangle$ transition at 5eV in a harmonic oscillator. (a) shows the frequency response at a constant source-to-absorber distance of 10 nm and (b) shows the distance dependence at resonance (5 eV).

spin is broken and the matrix element for the $S_z = 0$ triplet state [Eq. (D6)] also becomes nonzero.

APPENDIX E: ABSORPTION MATRIX ELEMENT FOR THE SIMPLE HARMONIC OSCILLATOR

For comparison with the results presented in the main text, in this section we show the absorption matrix elements of a model system with single-particle localized eigenstates. We choose a ubiquitous reference system, i.e., the quantum simple harmonic oscillator (SHO). The SHO is defined by the Hamiltonian $H = \frac{p^2}{2m_e} + \frac{1}{2}m_0\omega^2 r^2$ where the energy eigenvalues are given by $E_{n_x, n_y, n_z} = \hbar\omega(n_x + n_y + n_z + \frac{1}{2})$, $n_{x/y/z}$ being the quantization number along X , Y , and Z , and the eigenfunctions are given by the Hermite polynomials \mathcal{H} , i.e., $\langle r|\phi_{n_x, n_y, n_z}\rangle \propto \mathcal{H}_{n_x}(x)\mathcal{H}_{n_y}(y)\mathcal{H}_{n_z}(z)$ with appropriate normalization. The energy spacing between the ground state $|\phi_{0,0,0}\rangle$ and the z -polarized first excited state $|\phi_{0,0,1}\rangle$ is $\hbar\omega$ which we equate to 5eV to match the absorption line of the F center in MgO. We then compute the matrix element between $|\phi_{0,0,0}\rangle$ and $|\phi_{0,0,1}\rangle$: $v_{k,\alpha_S}^{(A)} = \langle\phi_{0,0,1}|H_{\text{int}}|\phi_{0,0,0}, 1_{k\alpha_S}\rangle/\sqrt{\Delta k}$. Such a transition has, by definition, an oscillator strength of 1.

As expected, in Fig. 11(a) it is apparent that the $\bar{A} \cdot \bar{p}$ and $e\bar{E} \cdot \bar{r}$ matrix elements are only equivalent at resonance. For the simple harmonic oscillator, the electron Hamiltonian is of the type of $H_A = \frac{p^2}{2m_0} + V(r)$, hence the commutation relation $[H, \bar{r}] = \bar{p}$ holds which makes the two matrix elements equal at resonance ($\omega_k = \omega_A$). We further note from Fig. 11(b) that the equality between the $\bar{A} \cdot \bar{p}$ and $e\bar{E} \cdot \bar{r}$ matrix elements at resonance extend at both the near-field and far-field regimes. This is unlike the matrix element between the Kohn-Sham orbitals of the V_O : MgO defect shown in Fig. 2 of the main text, for which the Hamiltonian is nonlocal and thus the $\bar{A} \cdot \bar{p}$ and $e\bar{E} \cdot \bar{r}$ matrix elements are not equivalent.

APPENDIX F: DENSITY FUNCTIONAL THEORY CALCULATION OF THE ORBITALS

We estimated the wave functions of the localized s and p orbitals of the V_O : MgO (as shown in Fig. 2) using Kohn-Sham DFT using the QUANTUM ESPRESSO package [30]. We

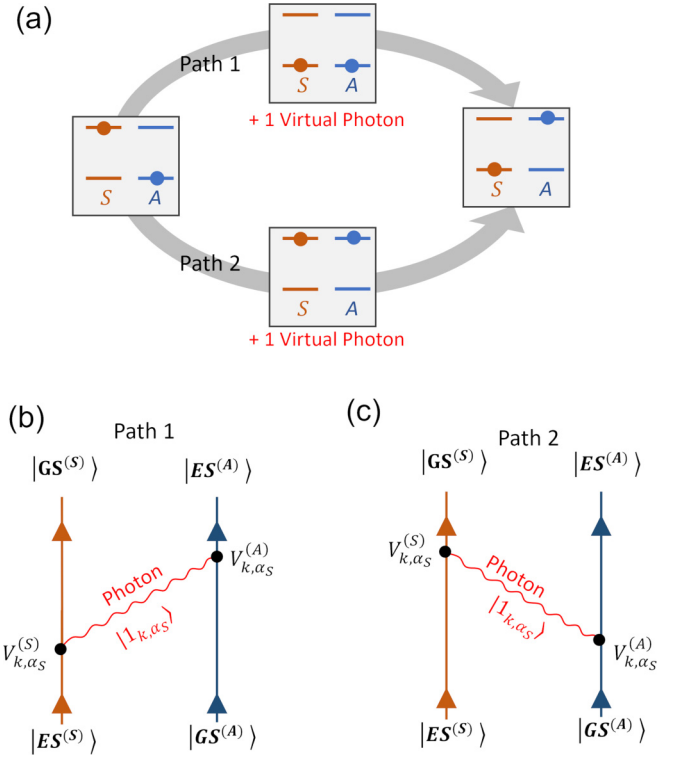


FIG. 12. (a) Two possible paths for the energy transfer from S to A, with respective Feynman diagrams shown in (b) and (c).

used the SG-15 norm-conserving Vanderbilt pseudopotentials [61,79]. We used both the Perdew-Burke-Ernzerhof approximation (PBE) [80] and dielectric dependent hybrid (DDH) [81] exchange correlation functionals and we found that this choice does not significantly affect the shape and localization of the defect orbitals, as indicated in Fig. 2 of the main text. There are several many body perturbation theory approaches to estimate the absorption and emission energies of the transitions [36,37,38]. However, in our calculations we simply take the known experimental value of 5 eV as the absorption energy in the transition of interest.

APPENDIX G: SOLUTION OF ENERGY TRANSFER UNDER SECOND-ORDER PERTURBATION

We start with emitter S in the excited state at time $t = 0$ and derive the probability amplitude for the energy transfer to the absorber A as a function of time within second-order perturbation theory.

We consider two possible paths [Fig. 12(a)]. In path 1, the source S emits a photon and transitions from an excited state to the ground state and the photon is absorbed in A. This is shown in the Feynman diagram in Fig. 12(b). The interaction terms for this path come from the first term of the interaction Hamiltonian in Eq. (B7). In path 2 [Fig. 12(c)], the time ordering of the photon absorption and emission events are reversed. In our case path 2 does not contribute to any NRET amplitude and only the contribution of path 1 provides the transfer amplitude [4,5].

The overall NRET amplitude $c(t)$ can be expressed as

$$c(t) = \langle \Psi_f | \mathcal{T} \left\{ \exp \left(-\frac{i}{\hbar} \int_0^t dt' \tilde{H}_{\text{int}}(t') \right) \right\} | \Psi_i \rangle. \quad (\text{G1})$$

Here $\tilde{H}_{\text{int}}(t') = e^{\frac{iH_0 t'}{\hbar}} H_{\text{int}}(t') e^{-\frac{iH_0 t'}{\hbar}}$ where $H_{\text{int}}(t')$ is from Eq. (2) and $H_0 = H_A + H_B + H_{\text{Field}}$ is the Hamiltonian of the unperturbed system. The initial state is $|\Psi_i\rangle = |\Psi(t=0)\rangle = |ES^{(S)}\rangle |GS^{(A)}\rangle$; and the final state is $|\Psi_f\rangle = |GS^{(S)}\rangle |ES^{(A)}\rangle$. \mathcal{T} represents time-ordering of the operators. Using second-order perturbation theory, we obtain

$$c^{(2)}(t) = e^{-i\omega_A t} \left(-\frac{i}{\hbar} \right)^2 \int_0^t dt' \int_0^{t'} dt'' \sum_I \langle \Psi_f | \tilde{H}_{\text{int}}(t') | I \rangle \langle I | \tilde{H}_{\text{int}}(t'') | \Psi_i \rangle. \quad (\text{G2})$$

The sum is over all possible intermediate states, which, for the positive time solution [path1, Figs. 12(a) and 12(b)] is given by $|I\rangle = |GS^{(S)}\rangle |GS^{(A)}\rangle |1_{k,\alpha_S}\rangle$. Thus, the evaluation of the NRET amplitude rests on the evaluation of the photon emission and absorption matrix elements denoted by $\langle I | \tilde{H}_{\text{int}}(t') | \Psi_i \rangle$ and $\langle \Psi_f | \tilde{H}_{\text{int}}(t') | I \rangle$ above. We calculate these matrix elements using wave functions obtained from first-principles electronic structure theory based on DFT, as discussed in the main text. We have

$$\begin{aligned} c^{(2)}(t) &= -e^{-i\omega_A t} \frac{1}{\hbar^2} \sum_{k,\alpha_S} V_{k,\alpha_S}^{(S)} V_{k,\alpha_S}^{(A)} \int_0^t dt' \int_0^{t'} dt'' e^{-i(\omega_k - \omega_A)t' + i(\omega_k - \omega_S)t''} \\ &= -e^{-i\omega_A t} \frac{1}{\hbar^2} \sum_{k,\alpha_S} \Delta k v_{k,\alpha_S}^{(S)} v_{k,\alpha_S}^{(A)} \int_0^t dt' \int_0^{t'} dt'' e^{-i(\omega_k - \omega_A)t' + i(\omega_k - \omega_S)t''}. \end{aligned} \quad (\text{G3})$$

Note that the summation extends to all energies of the photon modes as well as all possible multipole modes of the photon. The summation in k can be converted to an integral in energies:

$$c^{(2)}(t) = \sum_k \Delta k c_k(t) = \int_0^\infty dk c_k(t) = \frac{n_i}{c} \int_0^\infty d\omega c_k(t). \quad (\text{G4})$$

Here $c_k(t)$ is the contribution of the photons of wave vector k and width Δk in k space.

Straightforward evaluation of Eq. (G3) yields

$$c_k(t) = \frac{1}{\hbar^2} \sum_\alpha v_{k_S,\alpha_S}^{(S)} v_{k_S,\alpha_S}^{(A)} \left(\frac{e^{-i\omega_S t} - e^{-i\omega_A t}}{\omega_A - \omega_S} - \frac{e^{-i\omega_k t} - e^{-i\omega_A t}}{\omega_A - \omega_k} \right). \quad (\text{G5})$$

Assuming a smooth function for $v_{k_S,\alpha_S}^{(S)}$ and $v_{k_S,\alpha_S}^{(A)}$, the k integral is done by using a contour integration approach resulting in

$$c(t) = \frac{2i\pi n_i}{\hbar c} \sum_{\alpha_S} v_{k_S,\alpha_S}^{(S)} v_{k_S,\alpha_S}^{(A)} \frac{\sin\left(\frac{\Delta\omega}{2}t\right)}{\Delta\omega} = \frac{2M \sin\left(\frac{\Delta\omega}{2}t\right)}{\hbar \Delta\omega}. \quad (\text{G6})$$

$M = \frac{i\pi n_i}{\hbar c} \sum_\alpha v_{k_S,\alpha_S}^{(S)} v_{k_S,\alpha_S}^{(A)}$ here is the NRET matrix element which is equivalent to the coupling energy between the source and the absorber due to all the photon modes. For a point dipole source and absorber, M reduces to the dipole-dipole coupling energy of dipole moments \bar{p}_1 and \bar{p}_2 separated by a distance \bar{R} and is given by

$$M(\bar{R}) = \bar{p}_1 \cdot \bar{G}(\bar{R}) \cdot \bar{p}_2 \quad (\text{G7})$$

with

$$\bar{G}(\bar{R}) = \frac{I - 3\hat{R} \otimes \hat{R}}{4\pi\epsilon R^3} + \frac{k^2 e^{ikR}}{4\pi\epsilon R} \left[\left(1 + \frac{ikR - 1}{k^2 R^2} \right) I + \left(\frac{3 - 3ikR - k^2 R^2}{k^2 R^2} \right) \hat{R} \otimes \hat{R} \right], \quad (\text{G8})$$

being the electromagnetic Green dyadic for a homogeneous medium. Equations (G7)–(G8) are commonly used in molecular QED [55] to calculate energy transfer within the dipole approximation. However, unlike the dipole-dipole coupling, Eq. (G6) accounts for all the multipole modes and uses the absorption and emission matrix elements derived from first-principles theory.

[1] Th. Förster, Zwischenmolekulare energiewanderung und fluoreszenz, *Ann. Phys.* **437**, 55 (1948).

[2] D. L. Dexter, A theory of sensitized luminescence in solids, *J. Chem. Phys.* **21**, 836 (1953).

- [3] D. L. Dexter and J. H. Schulman, Theory of concentration quenching in inorganic phosphors, *J. Chem. Phys.* **22**, 1063 (1954).
- [4] A. Salam, The unified theory of resonance energy transfer according to molecular quantum electrodynamics, *Atoms* **6**, 56 (2018).
- [5] G. A. Jones and D. S. Bradshaw, Resonance energy transfer: from fundamental theory to recent applications, *Front. Phys.* **7**, 100 (2019).
- [6] L. B. Hughes *et al.*, A strongly interacting, two-dimensional, dipolar spin ensemble in (111)-oriented diamond, [arXiv:2404.10075](https://arxiv.org/abs/2404.10075).
- [7] P. Stevenson *et al.*, Erbium-implanted materials for quantum communication applications, *Phys. Rev. B* **105**, 224106 (2022).
- [8] G. Liu and B. Jacquier (eds.), Spectroscopic properties of rare-earths in optical materials, in *Springer Series in Materials Science*, Vol. 83 (Springer, Berlin, 2005).
- [9] D. L. Andrews and D. S. Bradshaw, The role of virtual photons in nanoscale photonics, *Ann. Phys.* **526**, 173 (2014).
- [10] D. L. Andrews, A unified theory of radiative and radiationless molecular energy transfer, *Chem. Phys.* **135**, 195 (1989).
- [11] D. L. Andrews, Optical angular momentum: multipole transitions and photonics, *Phys. Rev. A* **81**, 033825 (2010).
- [12] K. Nasiri Avanaki, W. Ding, and G. C. Schatz, Resonance energy transfer in arbitrary media: Beyond the point dipole approximation, *J. Phys. Chem. C* **122**, 29445 (2018).
- [13] A. I. Popov, E. A. Kotomin, and J. Maier, Basic properties of the f-type centers in halides, oxides and perovskites, *Nucl. Instrum. Methods Phys. Res. Sect. B* **268**, 3084 (2010).
- [14] A. Shluger, Defects in oxides in electronic devices, in *Handbook of Materials Modeling*, edited by W. Andreoni, and S. Yip (Springer International Publishing, Cham, 2019), pp. 1–22.
- [15] M. K. Singh, A. Prakash, G. Wolfowicz, J. Wen, Y. Huang, T. Rajh, D. D. Awschalom, T. Zhong, and S. Guha, Epitaxial Er-Doped Y_2O_3 on silicon for quantum coherent devices, *APL Mater.* **8**, 031111 (2020).
- [16] R. C. Knighton, L. K. Soro, L. Francés-Soriano, A. Rodríguez-Rodríguez, G. Pilet, M. Lenertz, C. Platas-Iglesias, N. Hildebrandt, and L. J. Charbonnière, Cooperative luminescence and cooperative sensitisation upconversion of lanthanide complexes in solution, *Angew. Chem.* **134**, e202113114 (2022).
- [17] B. Golesorkhi, H. Nozary, A. Fürstenberg, and C. Piguet, Erbium complexes as pioneers for implementing linear light-upconversion in molecules, *Mater. Horiz.* **7**, 1279 (2020).
- [18] D. Matsuura, Red, green, and blue upconversion luminescence of trivalent-rare-earth ion-doped Y_2O_3 nanocrystals, *Appl. Phys. Lett.* **81**, 4526 (2002).
- [19] S. B. Altner, M. Mitsunaga, G. Zumofen, and U. P. Wild, Dephasing-rephasing balancing in photon echoes by excitation induced frequency shifts, *Phys. Rev. Lett.* **76**, 1747 (1996).
- [20] M. Mitsunaga, T. Takagahara, R. Yano, and N. Uesugi, Excitation-induced frequency shift probed by stimulated photon echoes, *Phys. Rev. Lett.* **68**, 3216 (1992).
- [21] M. Ruf, N. H. Wan, H. Choi, D. Englund, and R. Hanson, Quantum networks based on color centers in diamond, *J. Appl. Phys.* **130**, 070901 (2021).
- [22] J. Lee, V. Leong, D. Kalashnikov, J. Dai, A. Gandhi, and L. A. Krivitsky, Integrated single photon emitters, *AVS Quantum Sci.* **2**, 031701 (2020).
- [23] S. Castelletto and A. Boretti, Silicon carbide color centers for quantum applications, *J. Phys. Photonics* **2**, 022001 (2020).
- [24] G. Wolfowicz, F. J. Heremans, C. P. Anderson, S. Kanai, H. Seo, A. Gali, G. Galli, and D. D. Awschalom, Quantum guidelines for solid-state spin defects, *Nat. Rev. Mater.* **6**, 906 (2021).
- [25] G. D. Scholes and D. L. Andrews, Resonance energy transfer and quantum dots, *Phys. Rev. B* **72**, 125331 (2005).
- [26] S. Lu and A. Madhukar, Nonradiative resonant excitation transfer from nanocrystal quantum dots to adjacent quantum channels, *Nano Lett.* **7**, 3443 (2007).
- [27] A. J. Mork, M. C. Weidman, F. Prins, and W. A. Tisdale, Magnitude of the Förster radius in colloidal quantum dot solids, *J. Phys. Chem. C* **118**, 13920 (2014).
- [28] W. Kohn and L. J. Sham, Self-consistent equations including exchange and correlation effects, *Phys. Rev.* **140**, A1133 (1965).
- [29] P. Hohenberg and W. Kohn, Inhomogeneous electron gas, *Phys. Rev.* **136**, B864 (1964).
- [30] P. Giannozzi *et al.*, QUANTUM ESPRESSO: A Modular and open-source software project for quantum simulations of materials, *J. Phys.: Condens. Matter* **21**, 395502 (2009).
- [31] L. Reining, The GW Approximation: Content, successes and limitations, *WIREs Comput Mol Sci* **8**, e1344 (2018).
- [32] G. Onida, L. Reining, and A. Rubio, Electronic excitations: Density-functional versus many-body Green's-function approaches, *Rev. Mod. Phys.* **74**, 601 (2002).
- [33] M. Govoni and G. Galli, Large scale GW calculations, *J. Chem. Theory Comput.* **11**, 2680 (2015).
- [34] H. Ma, N. Sheng, M. Govoni, and G. Galli, Quantum embedding theory for strongly correlated states in materials, *J. Chem. Theory Comput.* **17**, 2116 (2021).
- [35] N. Sheng, C. Vorwerk, M. Govoni, and G. Galli, Green's function formulation of quantum defect embedding theory, *J. Chem. Theory Comput.* **18**, 3512 (2022).
- [36] C. Vorwerk and G. Galli, Disentangling photoexcitation and photoluminescence processes in defective MgO, *Phys. Rev. Mater.* **7**, 033801 (2023).
- [37] S. Verma, A. Mitra, Y. Jin, S. Haldar, C. Vorwerk, M. R. Hermes, G. Galli, and L. Gagliardi, Optical properties of neutral F centers in bulk MgO with density matrix embedding, *J. Phys. Chem. Lett.* **14**, 7703 (2023).
- [38] Y. Jin, V. W. Yu, M. Govoni, A. C. Xu, and G. Galli, Excited state properties of point defects in semiconductors and insulators investigated with time-dependent density functional theory, *J. Chem. Theory Comput.* **19**, 8689 (2023).
- [39] E. E. Jelley, Spectral absorption and fluorescence of dyes in the molecular state, *Nature (London)* **138**, 1009 (1936).
- [40] L. Stryer and R. P. Haugland, Energy transfer: A spectroscopic ruler, *Proc. Natl. Acad. Sci. USA* **58**, 719 (1967).
- [41] D. Klose, A. Holla, C. Gmeiner, D. Nettek, I. Ritsch, N. Bross, M. Yulikov, F. H.-T. Allain, B. Schuler, and G. Jeschke, Resolving distance variations by single-molecule FRET and EPR spectroscopy using rotamer libraries, *Biophys. J.* **120**, 4842 (2021).
- [42] F.-F. Kong *et al.*, Wavelike electronic energy transfer in donor-acceptor molecular systems through quantum coherence, *Nat. Nanotechnol.* **17**, 729 (2022).
- [43] D. A. Gállico and M. Murugesu, Controlling the energy-transfer processes in a nanosized molecular upconverter to tap into

- luminescence thermometry application, *Angew. Chem. Int. Ed.* **61**, e202204839 (2022).
- [44] A. Shukla, G. Kaur, K. J. Babu, A. Kaur, D. K. Yadav, and H. N. Ghosh, Defect-interceded cascading energy transfer and underlying charge transfer in europium-doped CsPbCl₃ nanocrystals, *J. Phys. Chem. Lett.* **13**, 83 (2022).
- [45] K. N. Avanaki and G. C. Schatz, Entangled photon resonance energy transfer in arbitrary media, *J. Phys. Chem. Lett.* **10**, 3181 (2019).
- [46] V. M. Kenkre and R. S. Knox, Generalized-master-equation theory of excitation transfer, *Phys. Rev. B* **9**, 5279 (1974).
- [47] J. Flick, C. Schäfer, M. Ruggenthaler, H. Appel, and A. Rubio, *Ab initio* optimized effective potentials for real molecules in optical cavities: photon contributions to the molecular ground state, *ACS Photonics* **5**, 992 (2018).
- [48] M. K. Svendsen, Y. Kurman, P. Schmidt, F. Koppens, I. Kaminer, and K. S. Thygesen, Combining density functional theory with macroscopic QED for quantum light-matter interactions in 2D materials, *Nat. Commun.* **12**, 2778 (2021).
- [49] M. Ruggenthaler, J. Flick, C. Pellegrini, H. Appel, I. V. Tokatly, and A. Rubio, Quantum-electrodynamical density-functional theory: bridging quantum optics and electronic-structure theory, *Phys. Rev. A* **90**, 012508 (2014).
- [50] J. Flick, N. Rivera, and P. Narang, Strong light-matter coupling in quantum chemistry and quantum photonics, *Nanophotonics* **7**, 1479 (2018).
- [51] W. Schülke, *Electron Dynamics by Inelastic X-ray Scattering. in Oxford Series on Synchrotron Radiation*, Vol. 7 (Oxford University Press, Oxford, 2007).
- [52] P. I. Richards, On the Hamiltonian for a particle in an electromagnetic field, *Phys. Rev.* **73**, 254 (1948).
- [53] R. G. Woolley, On the Hamiltonian theory of the molecule-electromagnetic field system, *Mol. Phys.* **22**, 1013 (1971).
- [54] E. A. Power and T. Thirunamachandran, On the nature of the Hamiltonian for the interaction of radiation with atoms and Molecules: $(E/mc)p \cdot A$, $-\mu \cdot E$, and all that, *Am. J. Phys.* **46**, 370 (1978).
- [55] R. Grinter and G. A. Jones, Resonance energy Transfer: The unified theory via vector spherical harmonics, *J. Chem. Phys.* **145**, 074107 (2016).
- [56] A. I. Akhiezer and V. B. Berestetskii, *Quantum Electrodynamics* (Interscience, New York, 1965), Chaps. I and III.
- [57] J. D. Jackson, *Classical Electromagnetism* (Wiley, New York, 1998), Chap. 9.
- [58] M. Stavola, D. L. Dexter, and R. S. Knox, Electron-hole pair excitation in semiconductors via energy transfer from an external sensitizer, *Phys. Rev. B* **31**, 2277 (1985).
- [59] C. J. Pickard and F. Mauri, First-principles theory of the EPR g tensor in solids: Defects in quartz, *Phys. Rev. Lett.* **88**, 086403 (2002).
- [60] E. A. Power and T. Thirunamachandran, Quantum electrodynamics with nonrelativistic sources. I. transformation to the multipolar formalism for second-quantized electron and Maxwell interacting fields, *Phys. Rev. A* **28**, 2649 (1983).
- [61] D. R. Hamann, Optimized norm-conserving Vanderbilt pseudopotentials, *Phys. Rev. B* **88**, 085117 (2013).
- [62] J. C. Slater, The theory of complex spectra, *Phys. Rev.* **34**, 1293 (1929).
- [63] E. U. Condon, The theory of complex spectra, *Phys. Rev.* **36**, 1121 (1930).
- [64] B. R. Judd, Correlation crystal fields for lanthanide ions, *Phys. Rev. Lett.* **39**, 242 (1977).
- [65] P. Novák, K. Knížek, and J. Kuneš, Crystal field parameters with Wannier functions: Application to rare-earth aluminates, *Phys. Rev. B* **87**, 205139 (2013).
- [66] D. J. Newman and B. Ng, The superposition model of crystal fields, *Rep. Prog. Phys.* **52**, 699 (1989).
- [67] Chapter 5, The mesoscopic nature of quantum dots in photon emission, edited by P. Michler, *Quantum Dots for Quantum Information Technologies. in Nano-Optics and Nanophotonics* (Springer International Publishing, Cham, 2017).
- [68] S. Kanai, F. J. Heremans, H. Seo, G. Wolfowicz, C. P. Anderson, S. E. Sullivan, M. Onizhuk, G. Galli, D. D. Awschalom, and H. Ohno, Generalized scaling of spin qubit coherence in over 12,000 host materials, *Proc. Natl. Acad. Sci. USA* **119**, e2121808119 (2022).
- [69] A. Gibson, R. Haydock, and J. P. LaFemina, Stability of vacancy defects in MgO: The Role of charge neutrality, *Phys. Rev. B* **50**, 2582 (1994).
- [70] G. P. Summers, T. M. Wilson, B. T. Jeffries, H. T. Tohver, Y. Chen, and M. M. Abraham, Luminescence from oxygen vacancies in MgO crystals thermochemically reduced at high temperatures, *Phys. Rev. B* **27**, 1283 (1983).
- [71] L. A. Kappers, R. L. Kroes, and E. B. Hensley, F⁺ and F['] centers in magnesium oxide, *Phys. Rev. B* **1**, 4151 (1970).
- [72] A. Gallo, F. Hummel, A. Irmeler, and A. Grüneis, A periodic equation-of-motion coupled-cluster implementation applied to F-centers in alkaline earth oxides, *J. Chem. Phys.* **154**, 064106 (2021).
- [73] J. Strand, S. K. Chulkov, M. B. Watkins, and A. L. Shluger, First principles calculations of optical properties for oxygen vacancies in binary metal oxides, *J. Chem. Phys.* **150**, 044702 (2019).
- [74] C. Sousa and F. Illas, On the accurate prediction of the optical absorption energy of F-Centers in MgO from explicitly correlated *Ab Initio* cluster model calculations, *J. Chem. Phys.* **115**, 1435 (2001).
- [75] E. Ertekin, L. K. Wagner, and J. C. Grossman, Point-Defect optical transitions and thermal ionization energies from quantum Monte Carlo methods: Application to the F-center defect in MgO, *Phys. Rev. B* **87**, 155210 (2013).
- [76] P. Rinke, A. Schleife, E. Kioupakis, A. Janotti, C. Rödl, F. Bechstedt, M. Scheffler, and C. G. Van de Walle, First-principles optical spectra for F centers in MgO, *Phys. Rev. Lett.* **108**, 126404 (2012).
- [77] J. Franck and E. G. Dymond, Elementary processes of photochemical reactions, *Trans. Faraday Soc.* **21**, 536 (1926).
- [78] E. Condon, A theory of intensity distribution in band systems, *Phys. Rev.* **28**, 1182 (1926).
- [79] M. Schlipf and F. Gygi, Optimization algorithm for the generation of ONCV pseudopotentials, *Comput. Phys. Commun.* **196**, 36 (2015).
- [80] J. P. Perdew, K. Burke, and M. Ernzerhof, Generalized gradient approximation made simple, *Phys. Rev. Lett.* **77**, 3865 (1996).
- [81] J. H. Skone, M. Govoni, and G. Galli, Self-consistent hybrid functional for condensed systems, *Phys. Rev. B* **89**, 195112 (2014).